# Observations of the Structure and Evolution of Hurricane Edouard (2014) during Intensity Change. Part I: Relationship between the Thermodynamic Structure and Precipitation

JONATHAN ZAWISLAK AND HAIYAN JIANG

*Florida International University, Miami, Florida*

GEORGE R. ALVEY III AND EDWARD J. ZIPSER

*University of Utah, Salt Lake City, Utah*

ROBERT F. ROGERS

*NOAA/Atlantic Oceanographic and Meteorological Laboratory/Hurricane Research Division, Miami, Florida*

JUN A. ZHANG

*NOAA/Atlantic Oceanographic and Meteorological Laboratory/Hurricane Research Division, and Cooperative Institute for Marine and Atmospheric Studies, Rosenstiel School for Marine and Atmospheric Sciences, University of Miami, Miami, Florida*

STEPHANIE N. STEVENSON

*University at Albany, State University of New York, Albany, New York*

(Manuscript received 7 January 2016, in final form 27 May 2016)

## ABSTRACT

The structural evolution of the inner core and near environment throughout the life cycle of Hurricane Edouard (2014) is examined using a synthesis of airborne and satellite measurements. This study specifically focuses on the precipitation evolution and thermodynamic changes that occur on the vortex scale during four periods: when Edouard was a slowly intensifying tropical storm, another while a rapidly intensifying hurricane, during the initial stages of weakening after reaching peak intensity, and later while experiencing moderate weakening in the midlatitudes. Results suggest that, in a shear-relative framework, a wavenumber-1 asymmetry exists whereby the downshear quadrants consistently exhibit the greatest precipitation coverage and highest relative humidity, while the upshear quadrants (especially upshear right) exhibit relatively less precipitation coverage and lower humidity, particularly in the midtroposphere. Whether dynamically or precipitation driven, the relatively dry layers upshear appear to be ubiquitously caused by subsidence. The precipitation and thermodynamic asymmetry is observed throughout the intensification and later weakening stages, while a consistently more symmetric distribution is only observed when Edouard reaches peak intensity. The precipitation distribution, which is also discussed in the context of the boundary layer thermodynamic properties, is intimately linked to the thermodynamic symmetry, which becomes greater as the frequency, areal coverage, and, in particular, rainfall rate increases upshear. Although shear is generally believed to be detrimental to intensification, observations in Edouard also indicate that subsidence warming from mesoscale downdrafts in the low- to midtroposphere very near the center may have contributed favorably to organization early in the intensification stage.

## 1. Introduction

The question of whether or not a tropical cyclone (TC) will intensify remains a challenge for both the forecasting and research communities. A diverse array of processes,

*Corresponding author address*: Jonathan Zawislak, Dept. of Earth and Environment, Florida International University, 11200 SW 8th St., AHC-5, Rm. 360, Miami, FL 33199.
E-mail: jzawisla@fiu.edu

spanning the environmental, vortex, convective, turbulent, and microphysical scales, can play a key role in determining the likelihood of intensification (Marks and Shay 1998; Rogers et al. 2013a). In terms of processes occurring on the vortex scale and smaller, these mechanisms can be grouped into symmetric and asymmetric components.

The symmetric processes focus on the cooperative interaction between the primary and secondary circulations, and the impact of symmetric diabatic heating on this interaction (Ooyama 1969, 1982; Schubert and Hack 1982; Nolan and Grasso 2003; Nolan et al. 2007). Asymmetric mechanisms can assume a variety of scales and causal factors. These factors include environmental vertical wind shear (e.g., Reasor et al. 2009; Molinari and Vollaro 2010; Reasor and Eastin 2012; Nguyen and Molinari 2012); moisture gradients in the environment of the TC and the penetration of dry air into the inner core (e.g., Dunion and Velden 2004; Shu and Wu 2009), particularly at weaker intensities (Braun 2010; Sippel et al. 2011; Braun et al. 2012); lateral mixing of vorticity, heat, and moisture across gradients at the eye–eyewall interface (e.g., Schubert et al. 1999; Kossin and Schubert 2001; Kossin and Eastin 2001; Cram et al. 2007); and diabatic heating within deep convection in the inner core (e.g., Rodgers et al. 1998; Kelley et al. 2004; Reasor et al. 2009; Guimond et al. 2010; Rogers et al. 2013b, 2015). The challenge in improving TC intensity forecasts is to identify how the vortex structure and intensity will evolve in the presence of these processes.

Environmental vertical wind shear is one of the dominant factors governing TC intensity change. Although vertical wind shear has been identified as positively influencing intensification in some instances, shear is generally associated with being detrimental to intensification (e.g., Merrill 1988; Molinari et al. 2004; Eastin et al. 2005; Molinari et al. 2006; Reasor et al. 2009; Molinari and Vollaro 2010). Some hypothesize that one negative effect of vertical shear is the "ventilation" of the warm core (Gray 1968; Frank and Ritchie 2001), which raises surface pressures, while other studies suggest dynamical consequences such as tilting of the vortex downshear (DeMaria 1996) or the differential vorticity advection by shear causing upper-level divergence and low-level convergence downshear (Bender 1997; Frank and Ritchie 1999, 2001). In contrast, those that argue that vertical shear can positively contribute to intensification typically focus on center reformation in the downshear convection (Molinari et al. 2004, 2006).

Shear also forces a wavenumber-1 asymmetry in low-level flow, vertical motion, and distribution of precipitation (Marks et al. 1992; Black et al. 2002; Chen et al. 2006; Nguyen and Molinari 2012; Reasor et al. 2013; Zhang et al. 2013; DeHart et al. 2014; Uhlhorn et al. 2014). Although the translation of the storm may also contribute toward producing asymmetry, when the vertical wind shear is of at least moderate strength ($>7.5\,\mathrm{m\,s^{-1}}$), Chen et al. (2006) find that the asymmetry in the precipitation distribution due to vertical wind shear dominates over that due to the storm motion. Chen et al. (2006) also observe that when the magnitude of the vertical wind shear is low ($<5\,\mathrm{m\,s^{-1}}$), the contribution to asymmetry due to storm motion (relative to the contribution from shear) increases, but predominantly at radii away from the storm center (i.e., in the outer rainband region); within 100 km, the precipitation asymmetry is similar to the moderate- to high-shear cases.

Vertical wind shear tends to produce a vertical motion dipole, in which ascent is predominant in the downshear semicircle and descent upshear (Jones 1995; DeMaria 1996). As such, precipitation is primarily initiated in the downshear-right (DSR) quadrant, advected cyclonically around the storm through the downshear-left (DSL) quadrant, and weakens and dissipates in the upshear-left (USL) and upshear-right (USR) quadrants. The convective available potential energy (CAPE), which is used as a proxy for convective instability, is largely consistent with the vertical motion and precipitation asymmetry; CAPE is found to generally be largest downshear (favorable for convection) and lowest upshear (Bogner et al. 2000; Molinari and Vollaro 2010; Molinari et al. 2012; Dolling and Barnes 2014), and decreases with decreasing radius toward the center, to near-neutral conditions near the center (Bogner et al. 2000). Such a distribution of precipitation also impacts the planetary boundary layer (PBL) thermodynamics, where low equivalent potential temperature ($\theta_E$) air is transported to the surface in convective downdrafts on the downshear side outside the radius of maximum winds (RMW; Riemer et al. 2010). The PBL $\theta_E$ can recover as the air continues to travel through the upshear side and warms and moistens through surface enthalpy fluxes (Cione et al. 2000; Molinari et al. 2013; Zhang et al. 2013).

The structure and evolution of the thermodynamic and kinematic fields of TCs in shear clearly play a role in governing the distribution of inner-core precipitation. Consequently, whether a TC is about to undergo intensification must also be related to the structure and distribution of inner-core precipitation. While deep convection is often identified as a key indicator of TC intensification (e.g., Kelley et al. 2004; Reasor et al. 2009; Guimond et al. 2010; Rogers et al. 2013b, 2015; Stevenson et al. 2014; Susca-Lopata et al. 2015), recent satellite-based studies (e.g., Jiang 2012; Kieper and Jiang 2012; Zagrodnik and Jiang 2014; Alvey et al. 2015; Rozoff et al. 2015; Tao and Jiang 2015) have also identified the occurrence of shallow and moderate precipitation (and convection) as a key indicator that intensification is occurring. From either
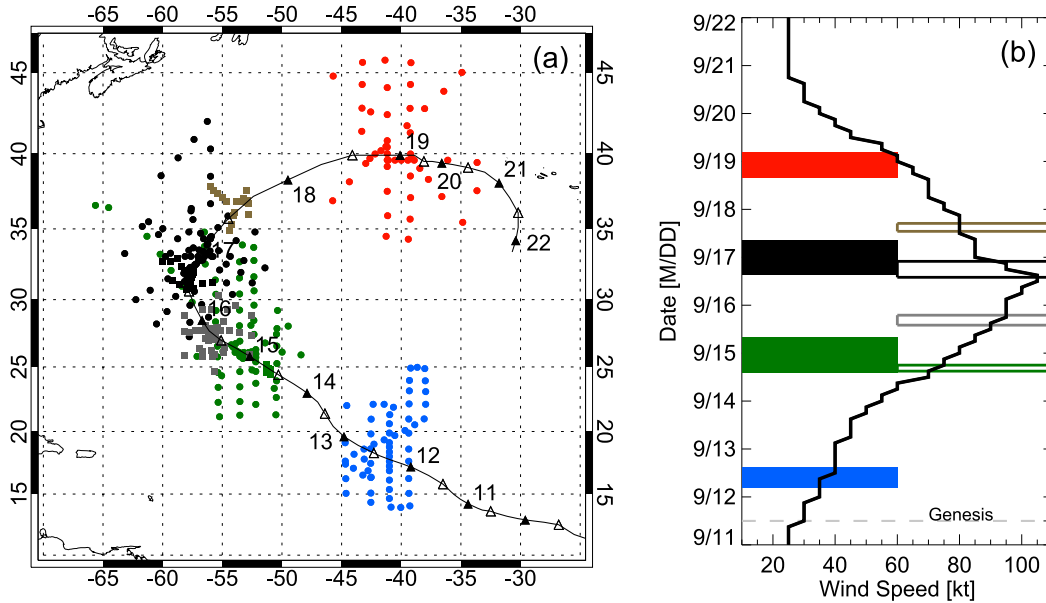
FIG. 1. (a) Map showing the location of each dropsonde observation from the GH (circle) and NOAA (square) aircraft, the 3-hourly interpolated best track (solid line) of Hurricane Edouard, the 0000 (solid triangle) and 1200 UTC (open triangle) positions (labeled by day in September); (b) timeline of best track maximum wind speed interpolated to 3-hourly with the on-station times (defined as first dropsonde to last dropsonde release) of each GH (solid bars) and NOAA (open bars) flight period (overlapping P-3 and G-IV missions are combined), as well as the genesis time (first TD classification, dashed line). Colors designate sampling periods that will be examined in this study.

perspective, the occurrence of precipitation upshear represents a favorable distribution for intensification, given that it promotes more symmetric diabatic heating around the center (Nolan et al. 2007; Stevenson et al. 2014; Zagrodnik and Jiang 2014; Chen and Gopalakrishnan 2015; Rogers et al. 2015). Considering that the most detrimental thermodynamic and kinematic conditions typically exist upshear, this finding suggests that the pathway to intensification seems to be intimately linked to a reversal of these unfavorable conditions (i.e., a reduction in the degree of wavenumber-1 asymmetry), and that precipitation plays an important role in this reversal. This study will analyze these processes for one particularly well-sampled intensification case.

In 2014, there were a series of aircraft missions into Hurricane Edouard that included flights with the National Oceanic and Atmospheric Administration (NOAA) WP-3D (P-3) and Gulfstream-IV (G-IV) aircraft, as a part of the NOAA Intensity Forecasting Experiment (IFEX; Rogers et al. 2006, 2013a), as well as with the National Aeronautics and Space Administration (NASA) unmanned Global Hawk (GH) aircraft, as part of the Hurricane Severe Storm Sentinel (HS3) field campaign (Braun et al. 2016). The GH is a high-altitude, long-endurance unmanned aircraft that was flown for up to 24 h and reached altitudes of up to 16.8–19.9 km (55 000–65 000 ft). Its utility was first demonstrated during the NASA

Genesis and Rapid Intensification Processes (GRIP) experiment (Braun et al. 2013) during 2010. Given the continuity of sampling Edouard over several days of its life cycle (Fig. 1), data from these aircraft offer a particularly unique opportunity to not only examine the structure at varying intensities, but also during various intensity change rates. Aircraft sampled the inner core and environment of Edouard during a period of slow intensification, rapid intensification to peak intensity, as well as throughout the weakening stage that immediately followed.

Airborne radar from the NOAA aircraft provides kinematic fields and information on the structure of the convection, while dropsondes provide thermodynamic profiles in the middle and lower troposphere. Dropsondes released from the GH, on the other hand, provide observations of the thermodynamic environment from ∼20 km (below ∼100 hPa) altitude down to the surface. These observations are used to document the structure and evolution of Edouard's warm core over several days, as well as describe the thermodynamic environment in the context of inner-core precipitation (and convective) properties (quantified using airborne radar and satellite-borne sensor datasets). Analyzing a synthesis of these observational datasets helps to address the importance of the mechanisms governing the azimuthal and radial distributions of precipitation and its role in the intensity evolution of Edouard.

This case study of Edouard consists of two parts. Part I provides an overview of Edouard and focuses on the evolution of the precipitation and deep-layer thermodynamic structure of Edouard, as revealed by high-altitude dropsondes and satellite microwave retrievals, over the course of several days. Both the warm-core structure and the relative humidity environment are discussed here in Part I, including the potential role that these structures played in the distribution of precipitation. Rogers et al. (2016, hereafter Part II) focus on the kinematic structure and distribution of deep convection, as revealed by airborne Doppler data, during two days in Edouard: one day when it was intensifying significantly, and another day when it had reached peak intensity and was beginning to slowly weaken. A discussion of some of the mechanisms underlying the radial and azimuthal distribution of deep convection during these two days is also presented in Part II.

## 2. Description of case and aircraft sampling

Edouard developed from a tropical wave that emerged off the African coast on 6 September (Stewart 2014). Several days later, at 1200 UTC 11 September, the wave was declared a tropical depression (TD6) about 2000 km east of the Caribbean Sea (Fig. 1a) and was upgraded to Tropical Storm (TS) Edouard 12 h later (at 0000 UTC 12 September). Edouard steadily intensified as it tracked west-northwest over the next several days, reaching hurricane status by 1200 UTC 14 September, which continued until 16 September when Edouard reached its peak intensity of 105 kt (1 kt = 0.5144 m s$^{-1}$). Almost immediately after reaching peak intensity, Edouard steadily weakened as it recurved toward the northeast in the central Atlantic, east of Bermuda.

Although sampling strategies varied among the flights, observations from the GH on 12 September were during a period of slow intensification (SI; ~10 kt day$^{-1}$) at tropical storm intensity (35–40 kt), while the observations from NASA and NOAA on 14 and 15 September were during a period of rapid intensification (RI[1];

---

[1] This rate is based on the best track information. Braun et al. (2016), however, offer evidence from P-3 and GH dropsonde data that there was a brief period (~9 h) on 14 September where Edouard's intensification rate likely far exceeded the rate given in the best track. Between 1500 UTC 14 September (P-3 observation) and 0032 UTC 15 September (GH), the estimated MSLP from the dropsonde observations decreases approximately 25 hPa. Over the same period in the best track, the MSLP only decreases 9 hPa. While the exact rate is less important to this study, the dropsonde observations validate that Edouard was likely undergoing RI during the P-3 and GH observing periods on 14–15 September, and is also relatively greater than the slower intensification rate observed on 12 September.

20–25 kt day$^{-1}$) (Fig. 1b). While observations from the GH and P-3 on 16 September (1200–1800 UTC) were close to the peak intensity (105 kt), Fig. 1b indicates that sampling occurred at the beginning stages of rapid weakening (rate approximately −20 to −25 kt day$^{-1}$). A single GH flight also sampled continued weakening from 70 to 55 kt on 18–19 September when Edouard was in the midlatitudes (40°N). The greatest gap in sampling was on 13 September, which unfortunately precedes Edouard's RI period. However, despite this gap, otherwise extensive sampling by multiple aircraft on 12 and 14–19 September allows for a detailed comparison of the structure of Edouard not only at different intensities, but also at various intensity change rates.

According to the deep-layer vertical wind shear (VWSH; Fig. 2a), which is defined as the difference between the mean wind vectors at 850 and 200 hPa within 500 km of the center from the Statistical Hurricane Intensity Prediction Scheme (SHIPS; DeMaria et al. 2005), during a period of initially slow intensification (12 September) Edouard was under the influence of moderate (8–10 m s$^{-1}$) south-southwesterly VWSH. It appears this shear direction is caused by the presence of an upper-level cold low to Edouard's west, as well as perhaps due to a midlatitude trough to its northeast, given that Edouard's outflow channel is visibly connected to this trough (not shown). Sea surface temperatures (SSTs[2]; Fig. 3) during this period were also only marginally favorable for intensification (~26°–27°C) (Kaplan and DeMaria 2003).

Over the next 2 days (13 and 14 September), however, an increasing intensification rate coincided with a relaxation in the VWSH (down to ~6 m s$^{-1}$) and warmer SSTs, which exceed 28.5°C over a large portion of the storm (Fig. 3). These favorable conditions persisted through 15 September, which allowed Edouard to steadily intensify to 105 kt. Beginning on 16 September, however, conditions became increasingly more conducive to weakening; SSTs steadily cool (Fig. 3) as the center tracks north of 40° latitude, while southwesterly shear increased (Fig. 2b) as Edouard interacted with an approaching midlatitude trough from the west.

## 3. Data and methodology

Table 1 provides a list of the NASA and NOAA research flights that are included in the analyses that follow, as well as the number of dropsonde observations

---

[2] SSTs are derived by Remote Sensing Systems from passive microwave data (4 and 11 GHz; Wentz et al. 2000) and are available daily at a 0.25° resolution.
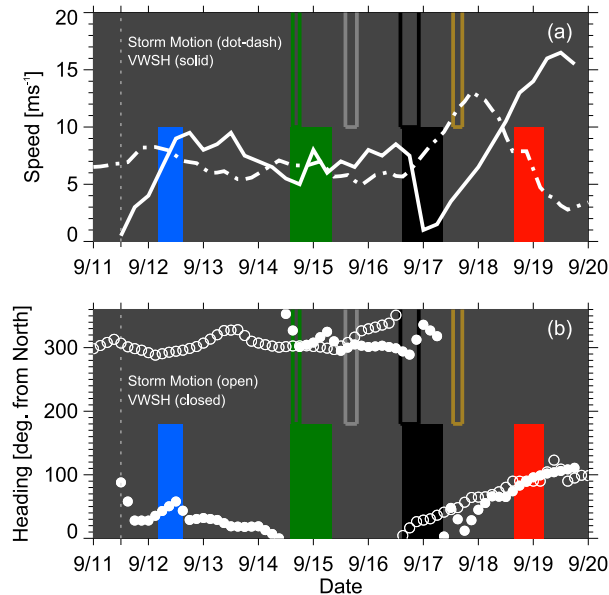
FIG. 2. Time series of (a) the storm motion speed computed from the best track and the magnitude of the 850–200-hPa vertical wind shear (VWSH) within 500 km from SHIPS (interpolated to 3-hourly), as well as (b) the storm motion and VWSH heading. Aircraft on-station times, consistent with Fig. 1, are also provided.

available from each flight. With the exception of near-surface quantities, analyses for all other variables shown are exclusively from the GH sample. The GH contributes 277 of the 386 observations (72% of the total sample) (UCAR/NCAR Earth Observing Laboratory 2015). The NOAA G-IV, which also cruises at a high altitude, only contributes 16 observations (4% of the total) during a single flight on 15 September, mainly outside of the inner core (>200 km). The P-3 aircraft provide daily samples between 14 and 17 September (93 total, or 24% of the total sample); however, because those profiles are confined to ~750 hPa and below, they are only included in analyses for near-surface quantities.

Variables measured directly by sensors on the drop-sonde package include the pressure, temperature, and relative humidity (RH), while the latitude, longitude, and wind speed and direction are derived from the GPS receiver. Other variables are computed for this study and include the potential temperature $\theta$, equivalent potential temperature $\theta_E$, and water vapor mixing ratio. The pseudoadiabatic CAPE without fusion and en-trainment is also computed for each profile, assuming parcels lifted from 100 m (Bogner et al. 2000; Molinari et al. 2012).

Each dropsonde profile is interpolated every 5 hPa from 1000 to 100 hPa. All GH profiles have been quality con-trolled by staff at the National Center for Atmospheric Research (NCAR) Earth Observing Laboratory (EOL)

(Young et al. 2016).[3] Quality control includes examining raw data (D-files) for data completeness and atypical fea-tures, and then a unique pressure correction is applied to each dropsonde profile (typically 1 hPa or less). Following the correction, geopotential altitude is computed from the GPS altitude, and the raw soundings are processed through the Atmospheric Sounding Processing Environment (AS-PEN) software (http://www.eol.ucar.edu/software/aspen), which applies final smoothing and removes suspicious data.

Unless otherwise noted, the latitude and longitude at each level of the profile is time/space adjusted to the nearest-in-time 3-hourly center location interpolated from the National Hurricane Center (NHC) best track using the storm motion speed of Edouard. The adjusted dropsonde locations, ro-tated with respect to shear, are shown in Fig. 4. Note that the color and symbol type of each observation corresponds to a particular agency aircraft (NOAA P-3, G-IV flights are combined) and observing period in the life cycle of Edouard, and is consistent with the color bars denoting the aircraft on-station times in Fig. 1b. These colors will be used consistently in all of the figures that follow. Note that while the locations in Fig. 4 are only the launch locations of each dropsonde, all analyses that follow in this study account for the horizontal drift of the dropsonde as it falls; therefore, at each pressure level, the location rotated with respect to shear can actually be in a different shear-relative quadrant from its location at a higher or lower altitude.

The analyses shown in this study do not differentiate between the individual contributions toward symmetry from VWSH and storm motion. Given that the magni-tude of the VWSH remains at least moderate ($\geq 6 \, \mathrm{m \, s^{-1}}$) throughout much of Edouard's life cycle (particularly during the intensification period) and that the asym-metric distribution due to storm motion and VWSH has previously been found to be largely similar at inner radii (Chen et al. 2006), VWSH is assumed to be dominant and analyses will only focus on the shear-relative distribution.

The spatial sampling of dropsonde observations from the GH flights in Edouard best accommodates an analysis of the vortex-scale thermodynamic changes

---

[3] The HS3 dropsonde dataset used in this study is the version 1 release by NCAR EOL. After the manuscript was accepted for publication, version 2 of the dataset was released, which corrected RH for a temperature-dependent dry bias, which was largest at colder temperatures (Young et al. 2016). Results were reproduced for version 2. While the mean RH in each shear-relative quadrant increased by approximately 5% at 400 hPa, 10% at 300 hPa, and 20% at 200 hPa, there is no noticeable difference in RH below 500 hPa and subsidence signatures in the upper troposphere re-main. The results and conclusions shown are, therefore, unaffected by this dry bias, and version 1 of the dataset was retained.
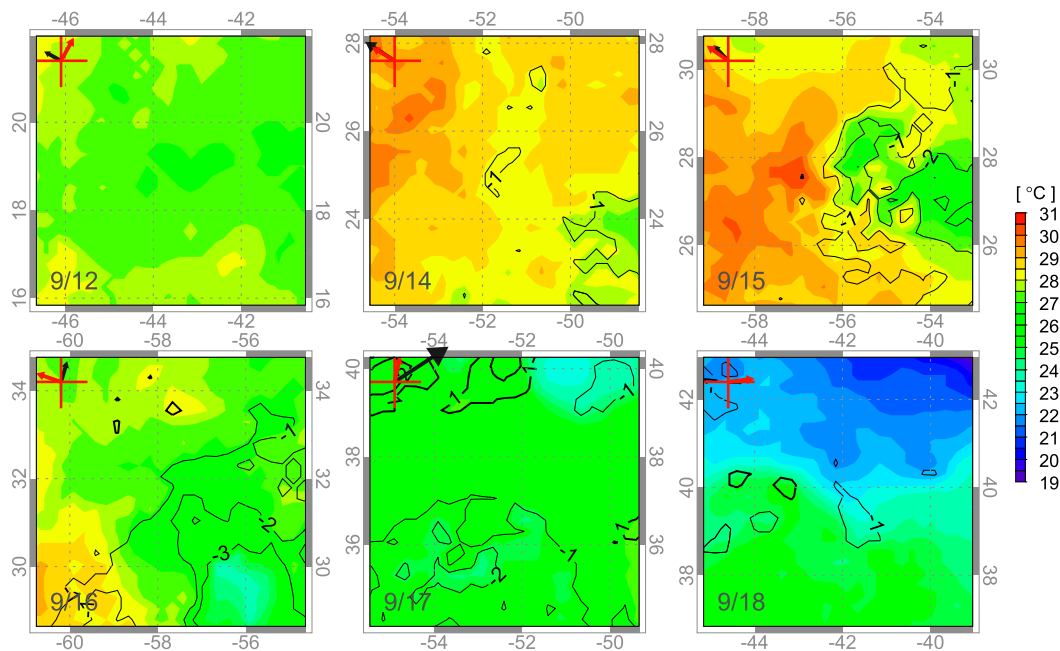
FIG. 3. Maps of the SST centered on the best track location daily at 1800 UTC. Line contours (thick, positive; thin, negative) indicate the anomaly from the SST on 11 Sep. The VWSH (red arrows) and storm motion (black arrows) headings are indicated, with the length of the motion vector shown proportional to the VWSH.

that occur in each shear-oriented quadrant (i.e., DSL, DSR, USR, and USL). In this study, the analysis is accomplished through the use of mean inner-core vertical profiles, defined as the average of observations within 200 km of the center[4] (shaded regions in Fig. 4). With few exceptions, the observations, at least from GH flights, are adequately spaced both azimuthally and radially to compare each shear-oriented quadrant from each flight (Fig. 4). An exception is the 18–19 September GH flight, which somewhat undersamples left of shear, and has a pattern more oriented along the shear vector.

## 4. Precipitation evolution

The evolution of precipitation in Edouard's inner core is qualitatively described using both conventional 30-min infrared (IR) data (Fig. 5), individual overpasses (Fig. 6) from passive microwave sensors (PMW), as well as lightning data from the World Wide Lightning Location Network (WWLLN) (Fig. 7).[5] PMW overpasses

shown in Fig. 6 include data from the Tropical Rainfall Measuring Mission (TRMM) Microwave Imager (TMI), Global Precipitation Measurement Mission (GPM) Microwave Imager (GMI), Special Sensor Microwave Imager/Sounder (SSMIS), and the Advanced Microwave Scanning Radiometer 2 (AMSR2). The brightness temperature ($T_B$) data are from the GPM level-1C algorithm (NASA GSFC 2010), which provides intercalibration of those sensors using GMI as the reference.

The IR (Fig. 5) and lightning (Fig. 7) time series suggest that deep convective pulses (peaks near 0000

---

[4] Smaller (100 km) and larger (300 km) averaging radii were also tested, and did not exhibit any notable differences.

[5] The detection efficiency of WWLLN over the North Atlantic is estimated to be 15%–25% (Rudlosky and Shea 2013; Stevenson et al. 2016), while the location accuracy is approximately 10 km (Abarca et al. 2010).

TABLE 1. Number of dropsonde observations for each Global Hawk (GH), NOAA P-3 (NOAA43 and NOAA42), and NOAA G-IV (NOAA49) flight included in the analysis.

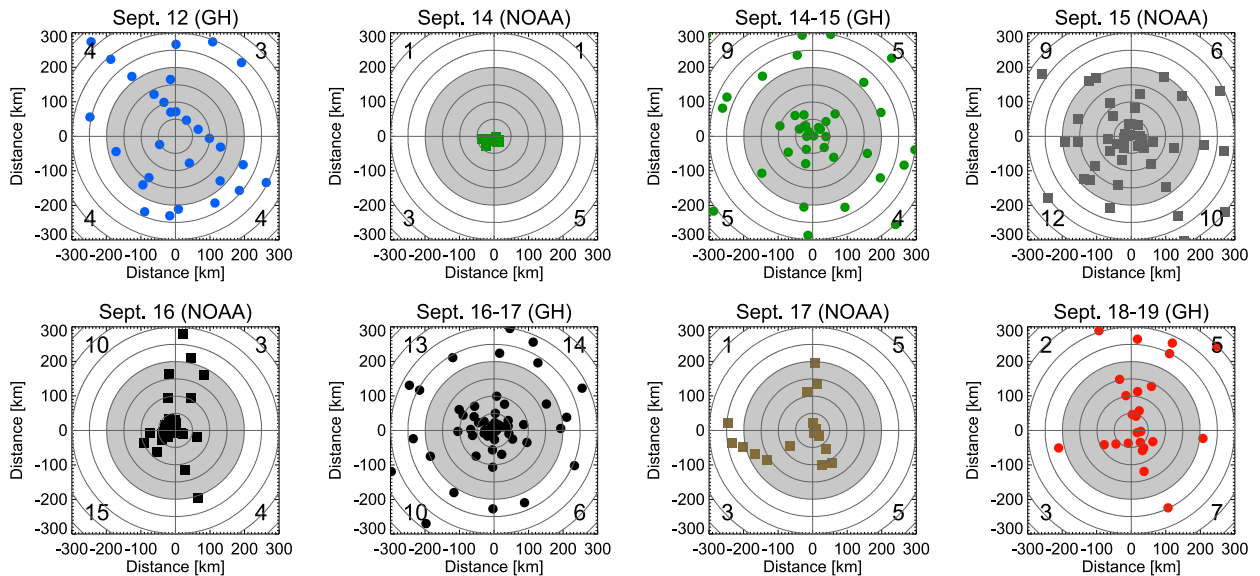| Aircraft | Date | No. of drops |
| --- | --- | --- |
| GH | 11–12 Sep | 60 |
| NOAA43 | 14 Sep | 8 |
| GH | 14–15 Sep | 80 |
| NOAA43 | 15 Sep | 19 |
| NOAA42 | 15 Sep | 14 |
| NOAA49 | 15 Sep | 16 |
| NOAA43 | 16 Sep | 23 |
| NOAA42 | 16 Sep | 12 |
| GH | 16–17 Sep | 87 |
| NOAA42 | 17 Sep | 17 |
| GH | 18–19 Sep | 50 |
| | Total | 386 |

FIG. 4. For each GH (circle) and NOAA (square) flight included (colors correspond to those in Figs. 1a,b), shown are the adjusted dropsonde locations relative to the nearest-in-time 3-hourly interpolated best track center, rotated with respect to shear. Shear heading direction is pointing upward, therefore the top-left quadrant is downshear left (DSL), top right is downshear right (DSR), bottom left is upshear left (USL), and bottom right is upshear right (USR). The area within 200 km is shaded gray, with the number of dropsonde observations within 200 km of the center in each quadrant indicated.

and 1200 UTC) are prevalent throughout the intensification period of Edouard (12–14 September), with the predominant occurrence of deep convection (proxy is cold cloud and lightning) in the downshear quadrants. Although they do not identify a clear diurnal cycle, Kossin (2002) has previously identified a semidiurnal signal in IR data within 100 km of the center of tropical storms and hurricanes. Dunion et al. (2014) do not identify a similar semidiurnal signal, although their dataset is restricted to major hurricanes and low to moderate shear cases ($<7.5 \, \mathrm{m \, s^{-1}}$). The upshear quadrants exhibit more variability in the occurrence of deep convection as cloud tops are generally warmer than the downshear quadrants, and there is also generally less lightning (particularly USR). The available PMW overpasses are consistent with this distribution; they indicate that the occurrence (i.e., area) of at least "moderate" precipitation[6] in the upshear quadrants during intensification is noticeably less than the downshear quadrants. Early in the intensification period (12–13 September), this distribution appears

to be driven, in part, due to stronger VWSH tilting the vortex downshear. The vertical tilt of the vortex is implied by comparing the best track centers (assuming these are accurate estimates of the surface circulation center) with the ones suggested at a higher altitude by the distributions of depressed 85–91-GHz PCT[7] seen in the sequences of PMW overpasses shown in Fig. 6.

Both the IR (Fig. 5) and PMW time series (Fig. 6) suggest that the precipitation symmetry increases (i.e., coverage increases USL and USR) as the VWSH decreases (Fig. 2a) and Edouard's intensification rate increases. The increase in symmetry also appears to coincide with a decrease in the vertical tilt of the vortex. Following Alvey et al. (2015), one way to quantify precipitation symmetry is to subtract the mean PCT (for all pixels with an 85–91-GHz PCT $< 250$ K within 1° radius of the center), or IR $T_B$, computed for each quadrant pair (i.e., DSL–USR, USL–DSR, etc.) and summing the total difference; as the value of the index decreases, the symmetry of the precipitation distribution increases. Figure 8 shows the symmetry index of each PMW overpass, as well as every 2 h from the IR,

---

[6] The proxy used for "moderate" precipitation is 85–91-GHz polarization corrected temperature (PCT) $\leq 250$ K, same as in Alvey et al. (2015). PCT is used instead of horizontal and vertical polarized brightness temperature since it resolves the ambiguity in separating the ocean background (low emissivity) from deep convective clouds (Spencer et al. 1989).

[7] Because depressed PCT at these frequencies is associated with ice scattering aloft, curvature in their distribution can reflect a higher altitude center.
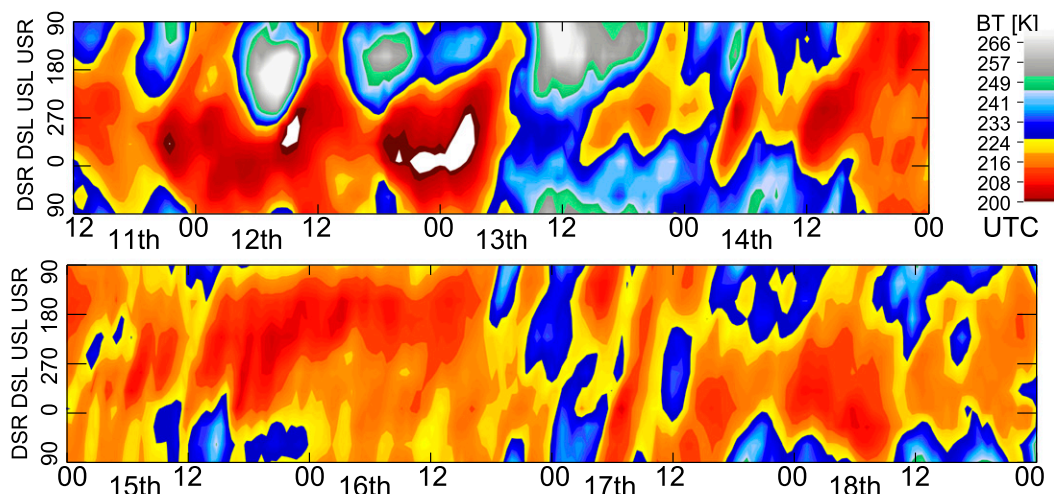
FIG. 5. Time series of 30-min infrared (IR) brightness temperature $T_B$ for the period between 1200 UTC 11 Sep and 0000 UTC 19 Sep, shown with respect to the shear-relative azimuth (shear heading is 0°); $T_B$ is averaged along each azimuth, over the inner 1 radial degree from the center. Shear quadrants are labeled: DSR (0°–90°), DSL (270°–0°), USL (180°–270°), and USR (90°–180°).

over Edouard. Consistent with composites produced using PMW (Alvey et al. 2015) and TRMM precipitation radar (Tao and Jiang 2015) data, this figure clearly shows the positive correlation between the precipitation symmetry and rate of intensity change. Following the initiation of a convective burst DSL around 2100 UTC 13 September, an increased occurrence (in duration and areal coverage) of upshear precipitation coincides with a greater intensification rate.

Although shallow, moderate, and deep precipitation is not specifically separated, Fig. 6 indicates that the areal coverage of 85–91-GHz PCT < 190 K, which serves as a proxy for deep convection, does not necessarily become symmetric and remains predominantly left of shear during intensification (also seen in the lightning data in Fig. 7). This location is similar to the composite shown in Alvey et al. (2015), and is consistent with the distribution of "very deep precipitation" (defined as 20-dB$Z$ echo ≥14 km) shown in Tao and Jiang (2015). In contrast, PCT most likely associated with a combination of shallow and moderately deep (85–91-GHz PCT of approximately 220–275 K) precipitation (convection) does become more symmetric (coverage increases upshear).

## 5. Thermodynamic evolution

### a. Relative humidity

The mean inner-core (within 200 km of the center) RH profiles for each shear-oriented quadrant are shown in Fig. 9 for each GH flight. The most noticeable difference among the quadrants is that the DSL and DSR quadrants show the

least change in RH during the intensification period (12–16 September). The greatest humidification (peak increase is ~15%) occurs at low- to midlevels (1000–650 hPa) between 12 and 14 September, which is consistent with those quadrants experiencing the most persistent precipitation between the two sampling periods (Figs. 5–7).

The USL and USR, in contrast, reveal a different time evolution than the downshear quadrants. Not only is the RH upshear generally lower during the SI period on 12 September, but the observations during the RI period on 14–15 September suggest that humidification at low to midlevels is more delayed than downshear, particularly USR. In the USR quadrant, the RH during both SI and RI is nearly identical, while a consistently more humid profile is not observed until Edouard reaches maturity (16–17 September). These results seemingly offer additional support for a close relationship between the humidity change and precipitation. In the upshear quadrants, the area, intensity, and persistence of precipitation (and deep convection), compared to downshear quadrants, is generally less (more variable) during the intensification (12–14 September) (Figs. 5–7), which logically explains the delayed increase in humidity. While the importance of low- to midlevel humidification for intensification has been identified previously (Kaplan and DeMaria 2003), this analysis suggests that *the relatively lower RH in the upshear quadrants, particularly USR, is initially the greatest hindrance to increasing precipitation symmetry, and must be overcome for the intensification of Edouard to proceed.*

Although transport of dry air into the core from the outer environment could be one source, the individual profiles ubiquitously show that subsidence is more likely
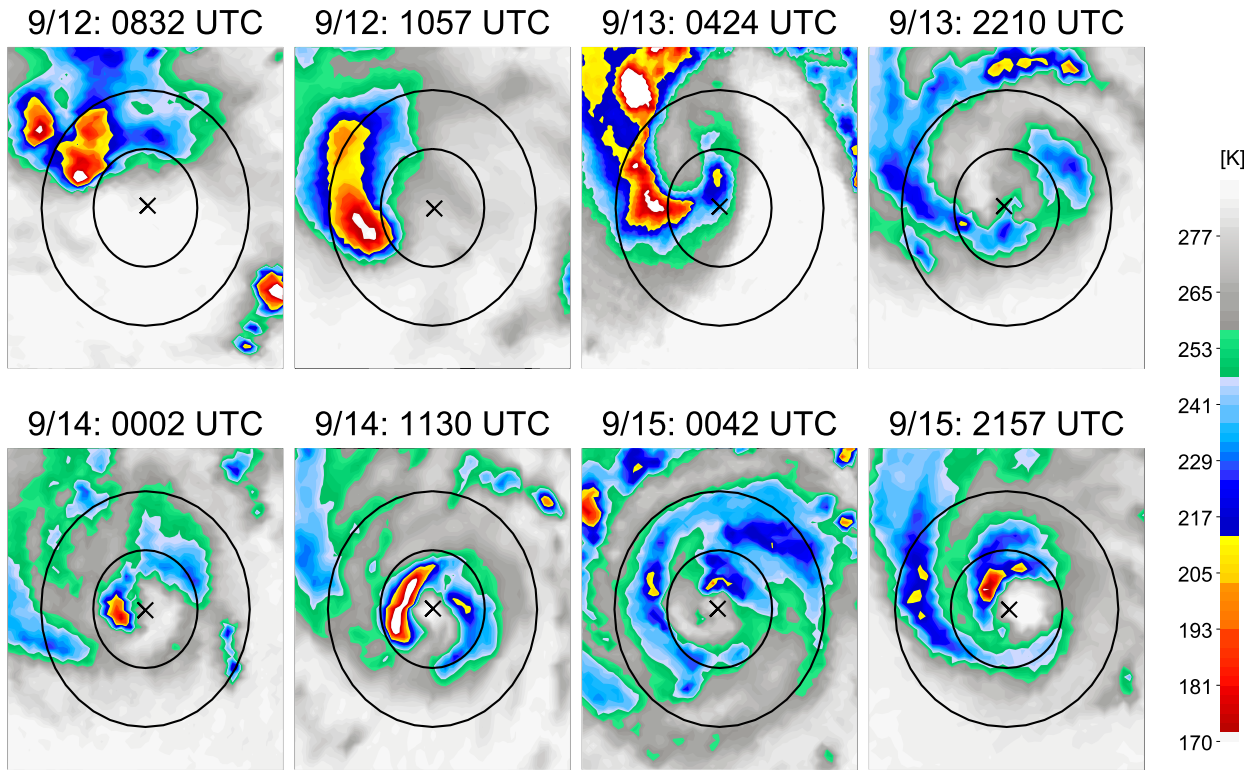
FIG. 6. The 85–91-GHz PCT from a selection of passive microwave overpasses rotated with respect to the shear-relative azimuth (shear heading is pointing up, or the 0° azimuth) during the intensification period of Edouard. Radial distances are 50 and 100 km from the interpolated best track centers (marked by "×").

responsible for these relatively (cf. downshear) dry layers upshear. Subsidence is identified in dropsonde profiles by the appearance of inversion layers where a sharp increase in potential temperature and decrease in water vapor mixing ratio indicates that adiabatic subsidence warming and drying is occurring. The presence of subsidence is consistent with the shear-induced wavenumber-1 asymmetry, in which there is a preference for dynamically forced (Jones 1995) and precipitation-driven (Black et al. 2002; Eastin et al. 2005; Reasor et al. 2013) descent in the upshear semicircle. Although the processes that generate relatively dry air in the low- to midtroposphere are considered less favorable for intensification, Section 6 will provide evidence that subsidence, in a preferred region near the developing center, may alternatively support a positive role toward organization during the early stages of intensification.

Mean RH profiles on 16–17 September (Fig. 9) are nearly identical in all quadrants, indicative that the RH finally achieves symmetry once the peak intensity of Edouard is reached. Weakening, however, immediately follows on 18–19 September as the VWSH increases (Fig. 2a) to a magnitude ($>10\,\mathrm{m\,s}^{-1}$) greater than any previous time during Edouard's life cycle.

As a consequence, the distribution of RH during that GH flight shows the most pronounced asymmetry. While the DSL quadrant remains relatively humid, all other quadrants are substantially drier (RH decreases as much as 60%). This pattern logically explains the precipitation asymmetry observed during rapid weakening shown in Tao and Jiang (2015) and Alvey et al. (2015). In
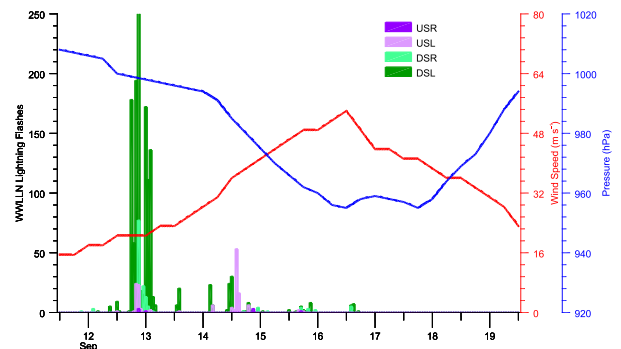


FIG. 7. Number of WWLLN lightning flashes within the inner 100 km between 1200 UTC 11 Sep and 1200 UTC 19 Sep, separated by shear-relative quadrant. The best track maximum wind speed (red) and MSLP (blue) are also shown. The center locations used for this analysis are interpolated from the best track to 1 min.
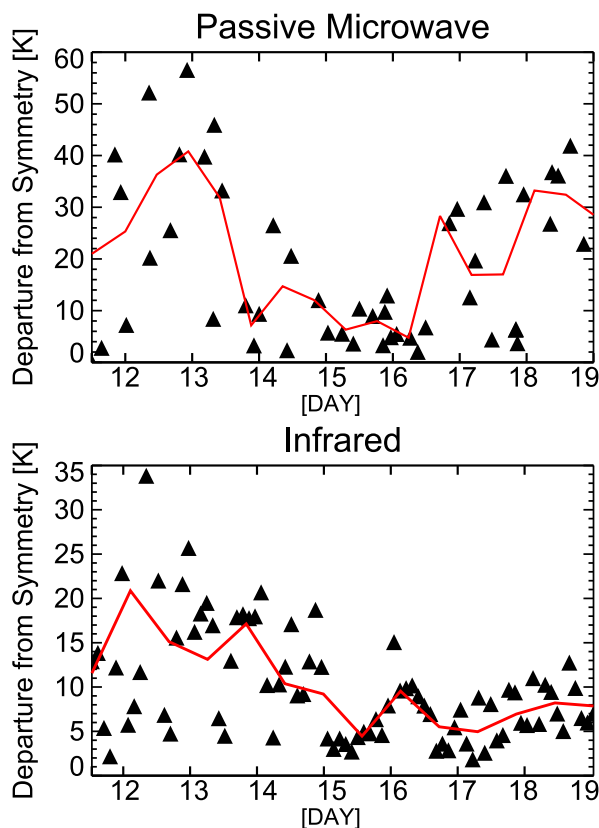
FIG. 8. Time series of the symmetry index, quantified within 1° of the center, (top) for each PMW overpass (excludes SSMI and only includes pixels with PCT < 250 K), as well as (bottom) computed every 2 h in the IR data. The red lines represent a 12-h running average of the data.

those composite satellite studies, weakening cases exhibit a precipitation maximum in the DSL quadrant, while substantially less precipitation occurs in all other quadrants.

### b. Equivalent potential temperature and instability

Figure 10 shows the mean inner-core profiles of $\theta_E$ for each GH flight. The DSL and DSR quadrants exhibit a pronounced increase in $\theta_E$ throughout the entire troposphere between the period of SI observed on 12 September and RI observed on 14–15 September. In addition to an increase in humidity (Fig. 9), at all levels both moistening (an increase in the water vapor mixing ratio; figure not shown) and warming, which can be implied by the temperature anomaly[8] (Fig. 11), appear

[8] The inner-core mean temperature anomaly is defined relative to the mean temperature profile of all observations within 300–700 km from the center for each GH flight. For brevity, the mean vertical profiles of potential temperature are not shown, but they also indicate warming throughout the troposphere during this period.

to be responsible for the increase in $\theta_E$. Likewise, similar to the result for RH, the upshear quadrants exhibit the most delayed increase in $\theta_E$, particularly at midlevels (700–500 hPa). As before, this result is consistent with the distribution and persistence of precipitation (more variable; Figs. 5 and 6) in these quadrants on 13 and 14 September. While the inner-core thermodynamic environment, particularly downshear, certainly appears more supportive of a greater intensification rate, an important conclusion from the GH observations on 14–15 September is that the thermodynamic (RH, $\theta_E$) and precipitation distributions remain asymmetric (Fig. 8), even though Edouard has intensified 25 kt in the previous 24 h, and is experiencing RI. The mean profile in the USR quadrant indicates no obvious increase in $\theta_E$ during the RI period, and only appears to achieve symmetry with the other quadrants once the peak intensity is reached (16–17 September).

Similar to observations taken by the P-3 on 14 September, which will be shown in more detail in Part II, dropsonde observations from the GH during the RI of Edouard (14–15 September) offer strong evidence that the DSR quadrant is the most favorable region for convective initiation. While both the DSL and DSR quadrants experience an increase of $\theta_E$ at all levels from the earlier SI stage (12 September), the vertical lapse rate of $\theta_E$ during the RI period remains larger DSR, and thus more convectively unstable; the difference between the near-surface $\theta_E$ and midlevel $\theta_E$ minimum is approximately 15 K in the DSR, while 7 K in the DSL. The CAPE values (Fig. 12) also verify that instability is favorable for convective growth as many of the observations in the DSR quadrant exceed 900 J kg$^{-1}$. This favorability appears to extend into the USR quadrant, but at radii farther from the center (150–300 km). The azimuthal distribution of CAPE within 200 km of the center is generally consistent with the composite results shown for outer radii (200–400 km) in Molinari et al. (2012); CAPE values are typically higher downshear than upshear.

The favorability for convective initiation DSR is even more revealing in the PBL properties. The maximum near-surface $\theta_E$ observed in any quadrant over the entire life cycle of Edouard occurs DSR during RI (Figs. 10 and 13a). This location is consistent with the composite PBL analyses shown in Zhang et al. (2013), and is a reflection of having warmer SSTs on 14 September than 2 days earlier (Fig. 3), as well as higher surface winds in the PBL that can support stronger surface fluxes. In addition to the thermodynamic favorability of the PBL, previous studies (Reasor et al. 2013; Zhang et al. 2013) also have shown that, of all shear-relative quadrants, the storm-relative radial inflow within the PBL is also typically the strongest and deepest in the DSR. Part II will
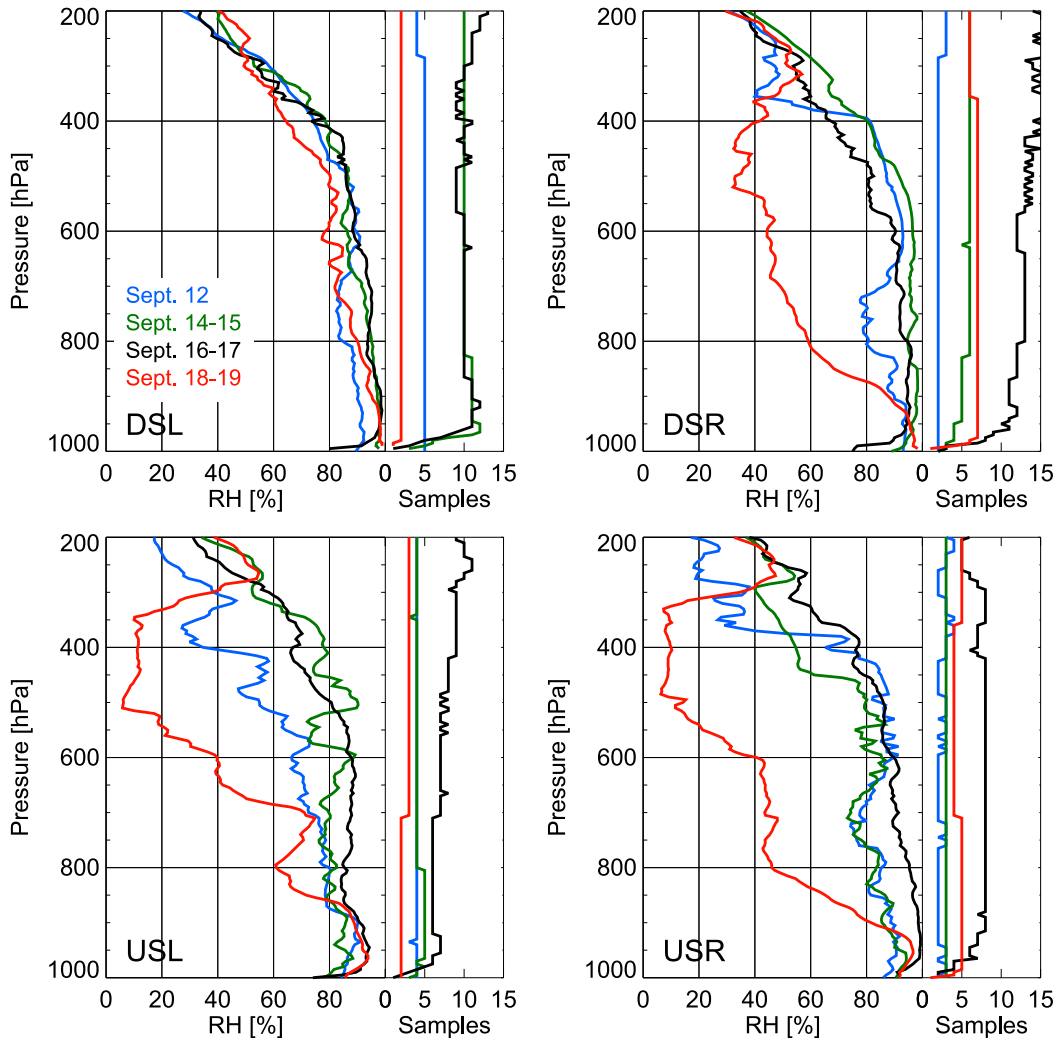
FIG. 9. The mean RH profile within 200 km of the center in each shear-oriented quadrant for each GH flight into Edouard; 12 Sep (blue), 14–15 Sep (green), 16–17 Sep (black), and 18–19 Sep (red). The number of samples contributing to each mean profile is shown on the right of each panel.

present evidence from a P-3 flight on 14 September that supports this favorable kinematic condition.

Although they typically exhibit a smaller $\theta_E$ lapse rate (Fig. 10) than DSR, observations in the DSL quadrant suggest that instability is still sufficiently favorable to support continued growth of convection originating from the DSR quadrant; many of the observations within the near inner core ($<$100 km) exceed 500 J kg$^{-1}$. However, despite having generally warmer SSTs than the DSR quadrant, DSL exhibits a relatively lower, and more stable, near-surface $\theta_E$ (Fig. 13).

Although dropsonde sampling along legs in the USL quadrant on 14–15 September is less than DSL (Fig. 2), the few observations available suggest that instability becomes increasingly less favorable for surface-based growth as convection rotates cyclonically into the USL

quadrant. Not only does the near-surface $\theta_E$ remain lower than right of shear, but the CAPE (Fig. 12) and mean $\theta_E$ profile (Fig. 10) are also generally lower USL compared to DSL, indicative of relatively drier air (Fig. 9) in the low to midlevels. Similar to the composite in Zhang et al. (2013), this result suggests an increase in stability in the low troposphere through the transport of cool, drier air to the surface in convective downdrafts.

Part II will present further kinematic evidence from the P-3 tail Doppler radar (TDR) and lower fuselage (LF) radars that, similar to other recent studies (Eastin et al. 2005; Hence and Houze 2011; Reasor et al. 2013; Zhang et al. 2013; DeHart et al. 2014; Tao and Jiang 2015), during the RI period of Edouard deep convection initiates DSR, achieves maturity DSL, and weakens as it propagates cyclonically through the upshear quadrants.
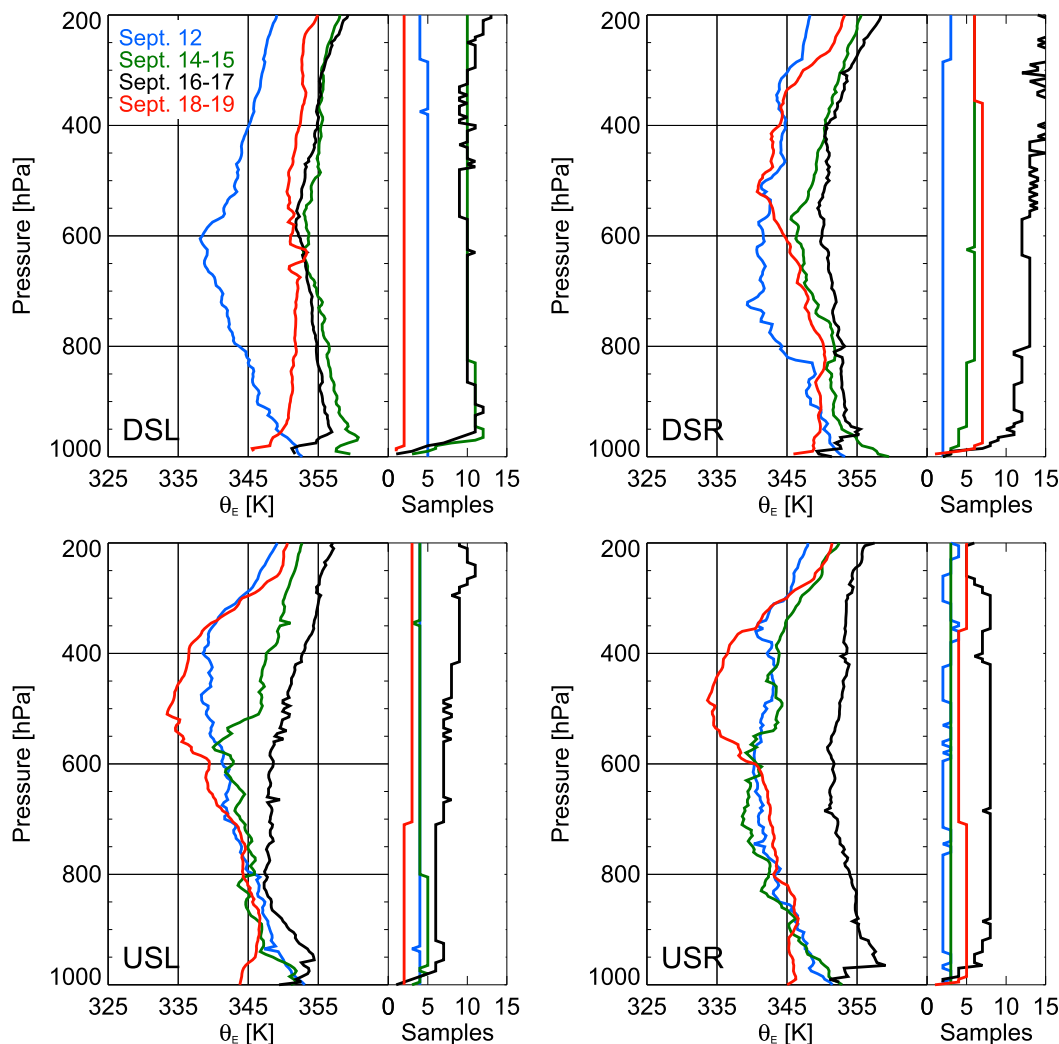
FIG. 10. As in Fig. 9, but for $\theta_E$.

This study uniquely shows that, on the vortex scale, the thermodynamic properties in the low to midtroposphere are not only consistent with this shear-induced precipitation asymmetry, but are also similar to the composite results of Zhang et al. (2013) (who do not differentiate by intensity or intensity change rate); the precipitation asymmetry observed during intensification is intimately linked to azimuthal variations of $\theta_E$ in the PBL.

On 16–17 September, soon after Edouard has reached peak intensity (maturity) (Fig. 1b). the mean profiles of RH (Fig. 9) and $\theta_E$ (Fig. 10) indicate that, in all quadrants, the inner core has reached near saturation (>90%) and convective instability has decreased in the free troposphere. This suggests that, on the vortex scale, thermodynamic symmetry has been achieved and eyewall convection, which is generally less intense than previous days (Figs. 5 and 7), is likely being primarily driven

by motion in a state of slantwise conditionally symmetric neutrality (Houze 2010) instead of buoyancy-driven instability. The observations, however, indicate some key symptoms of weakening. In addition to those symptoms observed in the kinematic properties (to be described in Part II), relatively cooler SSTs (<26°C; Fig. 3) are observed within the inner core, particularly in the quadrants right of shear. Figure 3 indicates that the SSTs in that part of the Atlantic basin on 16–17 September are not only relatively cool compared to those observed in that same region on 14 and 15 September, but are also cooler than the SSTs observed well in advance of Edouard's influence (11 September). This strongly suggests that, in addition to the typical decrease in SST with increasing latitude, storm-induced upwelling of cold water (e.g., Shay et al. 1992) is further contributing to a cool SST anomaly during the later stages (16–17 September). As a consequence of cooler
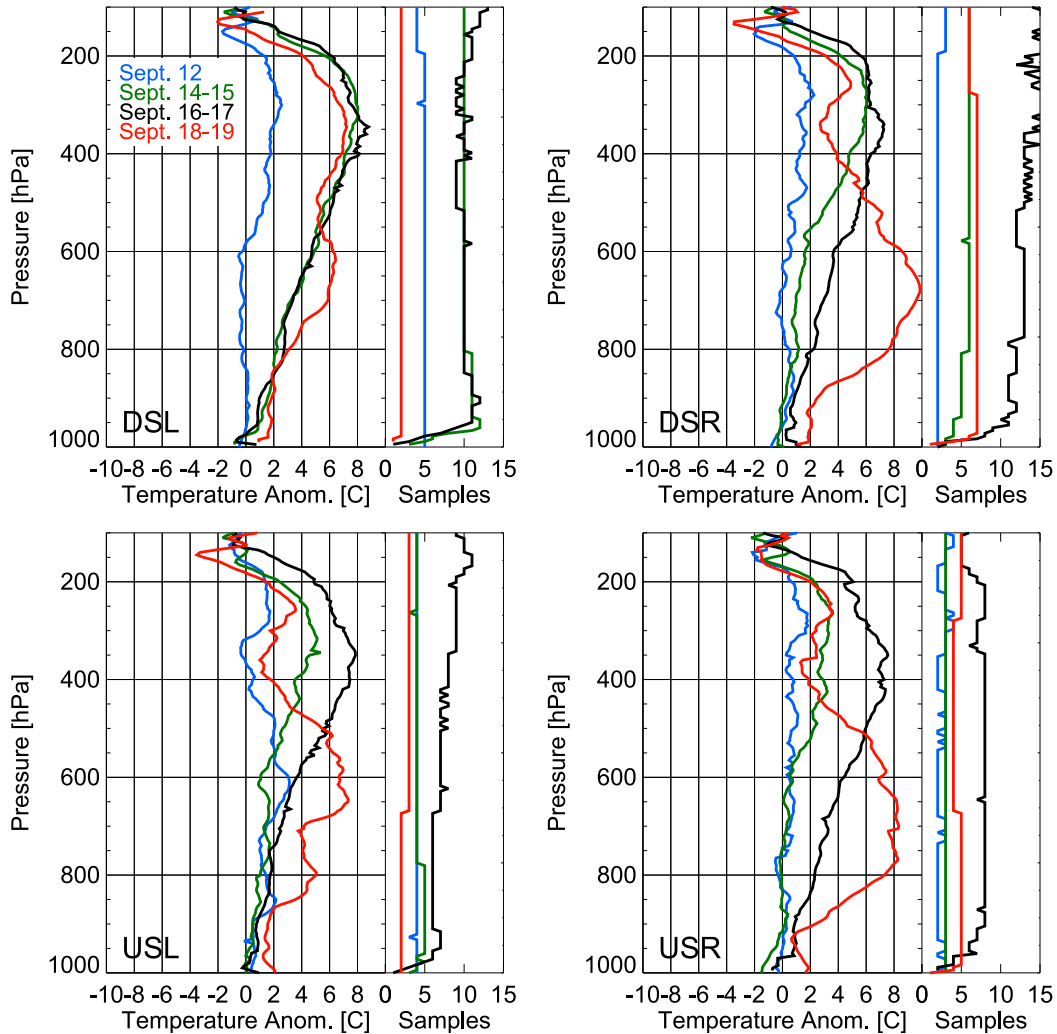
FIG. 11. As in Fig. 9, but for the temperature anomaly.

SSTs, surface fluxes are less likely to recover the low near-surface $\theta_E$ (Fig. 13c) generated by downdrafts, the near-surface layer is stabilized, and deep convection is subsequently less likely to be sustained or develop.

### c. Temperature anomaly

The temperature anomaly, defined as the difference between the mean temperature profile and a reference profile (i.e., the environmental profile), in each shear-oriented quadrant is also computed (Fig. 11). Similar to recent studies examining TC warm cores (Stern and Nolan 2012; Durden 2013), the reference profile is defined as the mean temperature profile of all observations within 300–700 km from the center for each GH flight. Figure 11 indicates that Edouard develops a robust warm anomaly, with a peak magnitude of 8°C that is maximized around 300 hPa. This height is generally consistent with cases included in Durden (2013) that

have a similar minimum sea level pressure (MSLP) as Edouard during its peak intensity (~960 hPa).

Similar to the RH and $\theta_E$ profiles, Fig. 11 indicates that an initially symmetric distribution among the quadrants on 12 September in the temperature anomaly transitions to a more asymmetric appearance during the RI period on 14–15 September. In the DSL quadrant, much of the warming is already achieved at RI onset, while in other quadrants, particularly USL and USR, the anomaly becomes progressively warmer during intensification, until once again achieving symmetry with the downshear mean profiles upon reaching maturity on 16 September. This evolution is even found when the mean profiles are defined for only dropsonde observations within 50 km (not shown). This result suggests that an asymmetric precipitation (downshear) distribution during intensification may bias the warming in the upper troposphere (above 600 hPa) toward downshear, and as
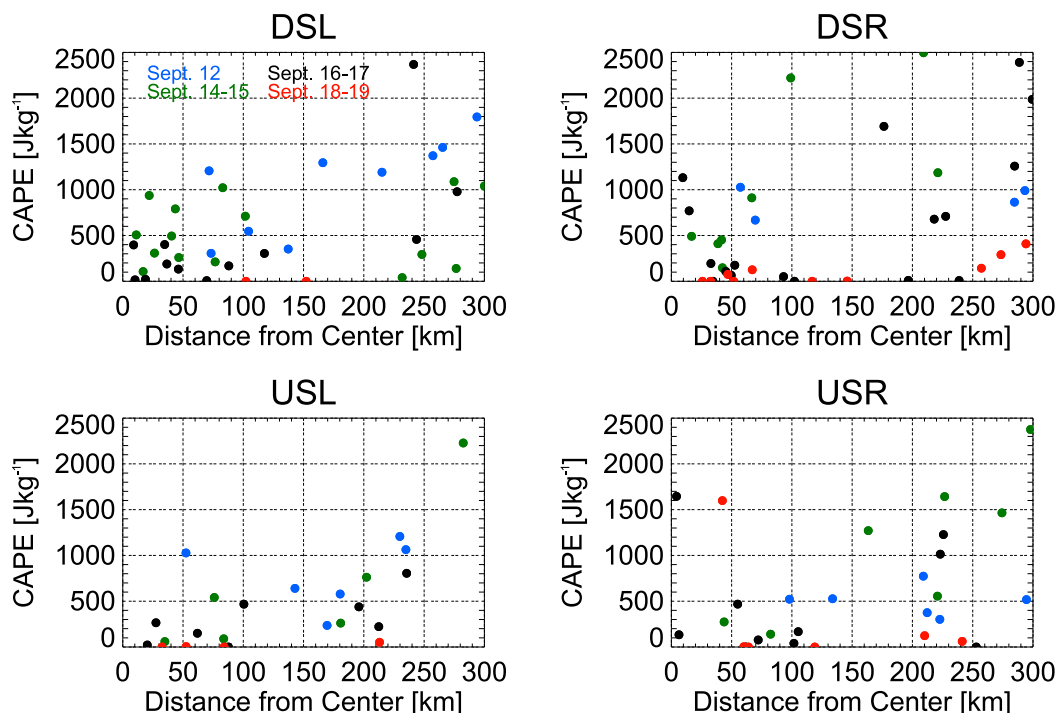
FIG. 12. The radial distribution of CAPE, computed from the dropsonde observations, for each GH flight in each shear-oriented quadrant. The shear-relative quadrant for each observation is determined by the location at 500 hPa.

the precipitation occurrence increases upshear so does the upper-tropospheric warming. This lends support to previous studies that hypothesize that intensification occurs as a response to an azimuthally averaged, or symmetric, latent heating (Ooyama 1969; Shapiro and Willoughby 1982; Nolan et al. 2007) mechanism, particularly when inside the RMW (Rogers 2010; Rogers et al. 2013b, 2015; Susca-Lopata et al. 2015). While this is true for the warming in the upper troposphere, evidence will be presented in the next section that warming in the midtroposphere is from another mechanism (subsidence), and may contribute differently to the intensification pathway.

## 6. Mechanisms for inner-core warming

This section will use individual GH transects to speculate on warming mechanisms within the inner core and, in particular, contrast between those responsible for warming in the upper troposphere (above 600 hPa) from those responsible in the low to midtroposphere. Transects from two GH flights will be shown, both of which represent typically undersampled periods during the TC life cycle: 1) 12 September, when Edouard is a weak tropical storm and slowly intensifying; and 2) on 18–19 September, when the storm is undergoing rapid weakening.

### a. 12 September

Figure 14 shows two of the three transects near the center of TS Edouard on 12 September. In the 5 h between these two transects (approximately 0845 and 1345 UTC) the best track indicates that Edouard slowly intensifies from 35 to 40 kt (Fig. 1b), with an accompanying decrease in MSLP from 1005 to 1000 hPa. Although the cross sections are somewhat offset from the center, the dropsonde observations are consistent with the best-track intensification rate as the lowest SLP observed in each transect is 1006 and 1000 hPa, respectively.

At 0845 UTC, the IR (Fig. 14) and PMW (Fig. 6) imagery suggests that precipitation is predominantly asymmetric, with the precipitation maximum located DSL. The location of the maximum upper-level warm anomaly (3°–4°C above 600 hPa) at 0845 UTC is located coincidentally with this maximum. In fact, the vertical profile of temperature anomaly within 250 km of the center in this quadrant appears consistent with the typical latent heating profile of stratiform raining areas; the observations are nearly saturated (not shown, but implied by the mean RH profile DSL in Fig. 9) throughout the troposphere with a warm anomaly above 600 hPa (melting level) and cooling below (in this case, up to −2°C).
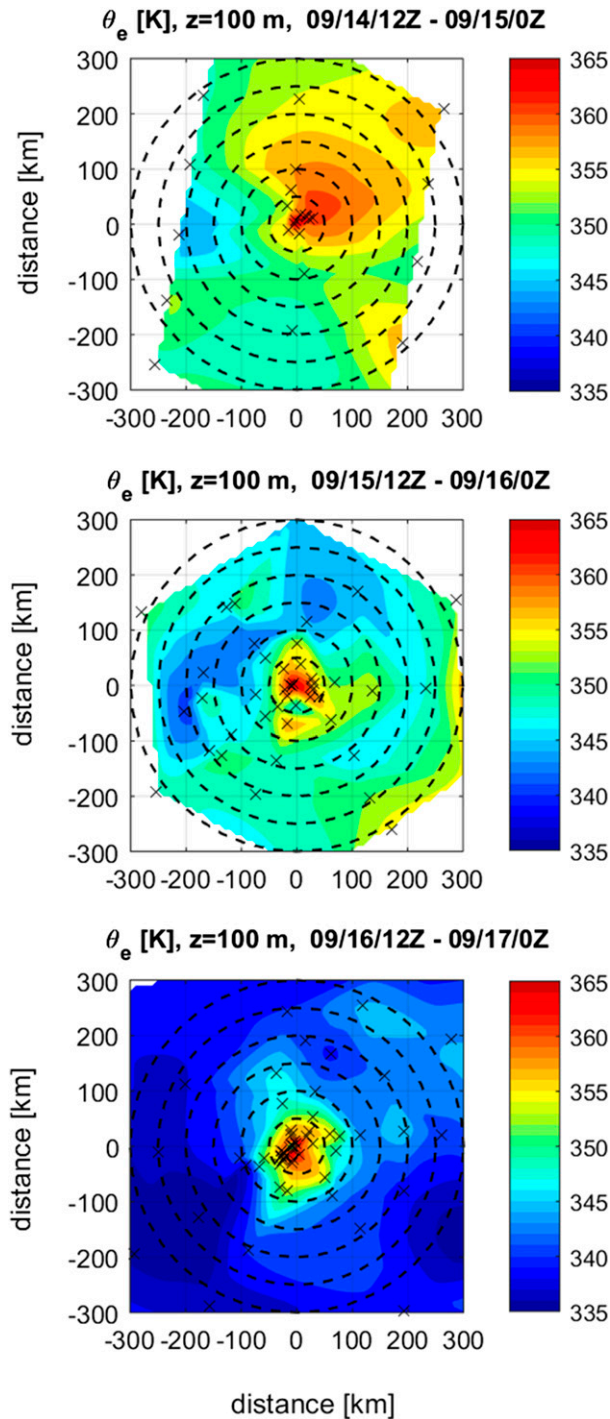
FIG. 13. Horizontal view of $\theta_E$ at 100-m altitude composited for three periods: (a) 1200 UTC 14 Sep–0000 UTC 15 Sep (both NOAA and GH dropsonde data contribute); (b) 1200 UTC 15 Sep–0000 UTC 16 Sep (NOAA only); (c) 1200 UTC 16 Sep–0000 UTC 17 Sep (both NOAA and GH). Data are rotated with respect to shear (shear heading pointing up, or the 0° azimuth). Also shown are the individual drop locations (''×''), as well as range rings every 50 km from the center.

Whereas the profiles strongly suggest latent heating is contributing to warming above 600 hPa in the DSL quadrant, an examination of observations in the USR portion of the transect suggests that subsidence is likely contributing to upper-level warming in that quadrant. Individual RH profiles along the transect indicate increasingly less humid profiles above 600 hPa with increasing distance from the center. The subsidence warming is maximized approximately 175 km from the center on the upshear side. Whether from latent heating or compensating subsidence induced from deep convection, broad upper-level warming, such as that seen in TS Edouard on 12 September, is generally recognized as an important pathway to intensification since, according to thermal wind balance, upper-level warming favors a lowering of the surface pressure (Zhang and Zhu 2012; Zhang and Chen 2012).

Case studies recently presented in Dolling and Barnes (2012) and Kerns and Chen (2015) identify a typically less discussed warming mechanism in the low to midtroposphere as an additional pathway to favorably reduce SLP, particularly when combined with warming at upper levels. In developing TCs, they identify regions of subsidence warming in the low to midlevels near the circulation center. A consequence of mesoscale unsaturated downdrafts in light stratiform raining areas (often characterized as ''onion soundings''; Zipser 1977), warming layers develop when cooling from evaporation below the melting layer is overcome by dry adiabatic compression. While the two dropsonde observations in the USR portion of the 0845 UTC transect (0856 UTC, shown in Fig. 15, and 0859 UTC), located in a relatively precipitation-free region just south of the deep convective maximum, cannot necessarily be classified as ''onion'' signatures, the profiles exhibit varying depths of relatively dry air (RH ~70%) compared to downshear quadrants, as well as symptoms of weak subsidence. The layers coincide with a weak warm anomaly (~1°C) at midlevels (850–650 hPa) that is favorably aligned with warming at upper levels, and are relatively close (~40 km) to the developing circulation center of Edouard.

By the next GH center crossing (1345 UTC), IR imagery indicates that the predominant area of cold cloud has rotated into the upshear quadrants. While the areal coverage of 215 K is relatively unchanged, the IR sequence (Fig. 5) indicates a general warming trend in IR $T_B$ and that deep convection ($T_B < 200$ K) is no longer present by the 1345 UTC crossing. This trend suggests that any precipitation present is likely stratiform. Collocated with this area is a more impressive onion signature, observed at 1339 UTC (Fig. 15) in the upshear portion of the center crossing. Although this transect is
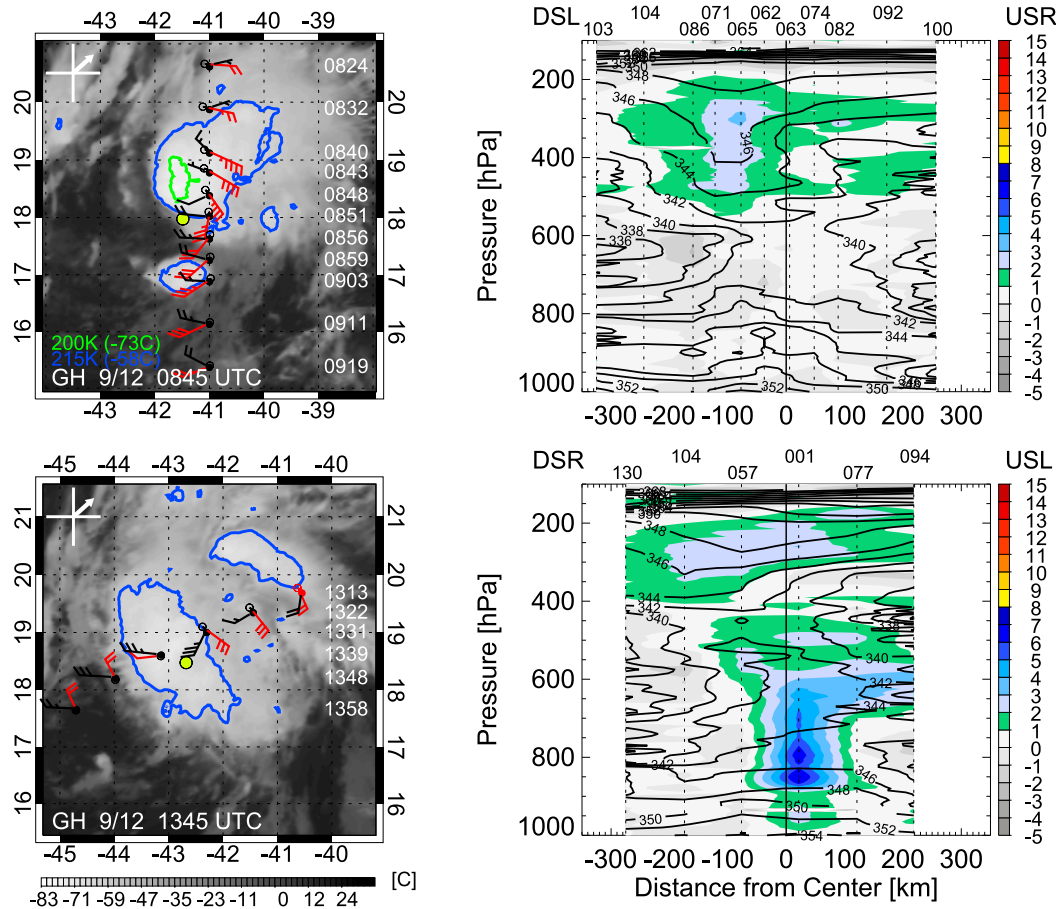
FIG. 14. (left) IR satellite image and (right) an accompanying cross section of thermodynamic data from drop-sonde observations from center transects by the GH at (top) 0845 and (bottom) 1345 UTC 12 Sep. The IR image (time shown at the bottom) shows the contours of 200- (green) and 215-K (blue) IR brightness temperature, the 2- (red) and 8-km (black) storm-relative wind barbs, interpolated center location (yellow dot) to the approximate crossing time, (top left) the 850–200-hPa VWSH heading, and the time of each dropsonde observation (listed on the right). The cross section contains the temperature anomaly (filled), $\theta_E$ (black contour, labeled every 2 K), sea level pressure (hPa; labeled at the top; lead "9" or "10" has been dropped), and the location (vertical dotted line) of the dropsonde observation. Distance is relative to the pseudocenter of the leg (i.e., the translation of the center onto the GH track). The quadrant relative to the VWSH of each inbound and outbound portion of the leg is also labeled in the top-left and top-right side of the cross section, respectively: DSL, DSR, USL, and USR.

through a somewhat different azimuth than at 0845 UTC (more oriented along the shear vector), at upper levels (above 400 hPa) the warm anomaly continues to suggest contributions from latent heating downshear and subsidence upshear. Compared to the more humid and weaker warm anomaly observed in the earlier near-center, upshear soundings (0856 and 0859 UTC), the observation at 1339 UTC has a midlevel RH (900–600 hPa) as low as 40% and is the largest observed warm anomaly (7°–8°C) of any observations on 12 September. Although the relationship of midlevel warming with intensification cannot be explicitly identified, the close proximity of midlevel warming (in conjunction with upper-level warming), most likely from subsidence, to

the developing center may favorably contribute to increasing the organization (slow intensification) of Edouard on 12 September.

### b. 18–19 September

Figure 16 shows transects from the GH at 1615 UTC 18 September and 0045 UTC 19 September, while Edouard is experiencing a moderate weakening rate (approximately $-15\,\text{kt}\,\text{day}^{-1}$). The main factors contributing to the weakening are the cooling SSTs (generally $<25°C$, Fig. 3) and increasing westerly shear, exceeding $10\,\text{m}\,\text{s}^{-1}$ (Fig. 2a). As should be expected given the westerly shear, the first transect at 1615 UTC shows an unfavorable eastward displacement of
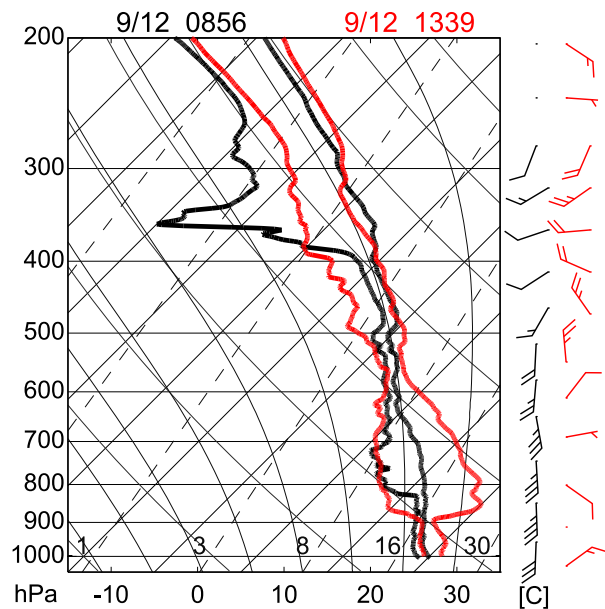
FIG. 15. Skew $T$–log$p$ profiles of the 0856 (black) and 1339 (red) UTC dropsonde observations on 12 Sep.

the cold cloud (and likely, precipitation) area from the low-level center. A misalignment of the vortex is also obvious; there is a progressive eastward displacement in the location of the vortex center from the surface (best track location), to 2- and 8-km centers (as approximated by the storm-relative winds). If the best track location is considered an accurate surface estimate, the misalignment between the surface and 8-km vortex center could be as large as 100 km.

The temperature anomaly structure at 1615 UTC indicates two separate areas of warming in the vertical; one located in the upper troposphere (above 500 hPa), primarily downshear of the low-level center, and another below 500 hPa (maximized near 700 hPa) on the upshear side of this transect. Given that the downshear anomaly coincides with the cold cloud area and the 8-km vortex center, this anomaly is likely the remnant warm core of Edouard. In contrast to downshear, the lower $\theta_E$ profiles upshear suggest that subsidence is drying and warming (as much as 9°–10°C compared to the environmental profile) over a deep layer (approximately between 750 and 250 hPa). Compared to the near-saturated profiles observed downshear, the RH upshear between 750 and 550 hPa is generally below 50%, and below 30% above 550 hPa.

In a later center crossing at 0045 UTC 19 September (8 h after the first one shown), according to the best track and the dropsonde observations, the MSLP has increased ~8–9 hPa, the maximum wind speed decreased 10 kt (70–60 kt) and, according to visible satellite imagery (not shown), the low-level circulation is exposed to

the west of the cold cloud shield. Further weakening is not surprising considering that the vertical misalignment of the lower- and upper-tropospheric warm anomalies have increased, while the anomaly below 500 hPa has warmed to nearly 13°C, suggesting that subsidence warming is suppressing convection upshear.

## 7. Conclusions

Part I of this two-part study has utilized a unique collection of dropsonde observations available from multiple NOAA P-3 (IFEX) and NASA (HS3) unmanned Global Hawk flights over the entire life cycle of Hurricane Edouard (2014) to investigate the precipitation evolution and thermodynamic changes that occur on the vortex scale during both the intensification and weakening stages. Particular focus was placed on the degree of symmetry of the shear-relative distribution of precipitation (as described using data from IR, fortuitous passive microwave overpasses, and WWLLN), RH, $\theta_E$, and temperature anomaly.

The precipitation distribution (Figs. 5–8), as well as the mean profiles shown for RH (Fig. 9) and $\theta_E$ (Fig. 10) in each shear-relative quadrant, is generally consistent with the wavenumber-1 asymmetry that has previously been observed in other sheared TCs (e.g., Marks et al. 1992; Jones 1995; Black et al. 2002; Molinari et al. 2012; Nguyen and Molinari 2012; Reasor et al. 2013; Zhang et al. 2013; Uhlhorn et al. 2014). This thermodynamic and precipitation asymmetry is observed throughout the intensification stage, even while Edouard is experiencing its most rapid intensification rate on 14–15 September. A consistently more symmetric distribution is not observed until 16–17 September, once Edouard has reached peak intensity. The wavenumber-1 asymmetry is most prominent during weakening (18–19 September) while vertical wind shear increases to over $10\,\mathrm{m\,s^{-1}}$ as Edouard recurves toward higher latitudes. During this observed weakening period, the vortex and upper-level warm core unfavorably tilt downshear with height, and midlevel warming from shear-induced subsidence dominates over the remnant low-level circulation.

Overall, the results indicate that the thermodynamic conditions in the upshear quadrants, particularly upshear right, are initially the greatest hindrance to increasing symmetry, and thus intensification, of Edouard. Intensification is intimately linked to the removal of unfavorable, relatively dry layers in the upshear quadrants that exist throughout the troposphere from a combination of dynamically forced (Jones 1995; DeMaria 1996) and precipitation-driven (Black et al. 2002; Eastin et al. 2005; Reasor et al. 2013) subsidence. Evidence from Edouard supports this process as the
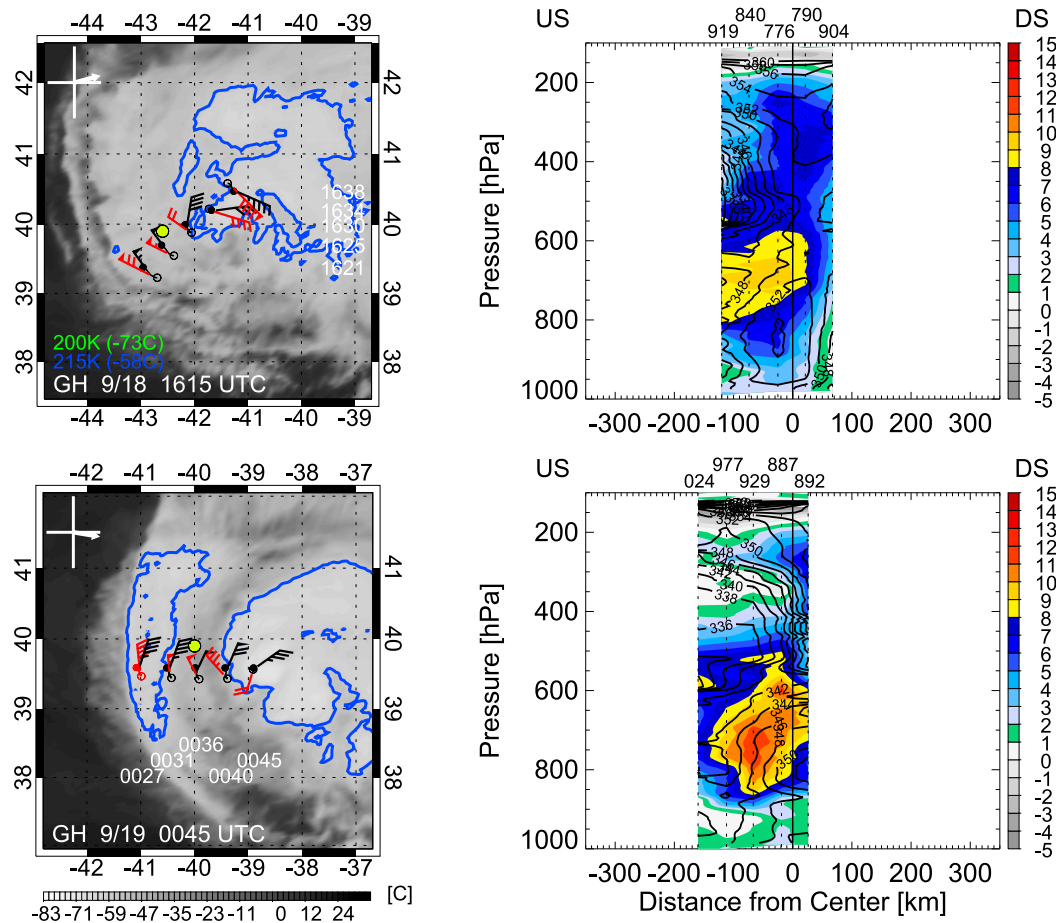
FIG. 16. As in Fig. 14, but for US (upshear) to DS (downshear) center transects by the GH at (top) 1615 UTC 18 Sep and (bottom) 0045 UTC 19 Sep.

upshear-right and upshear-left quadrants exhibited the most delayed humidification (Fig. 9), moistening (Fig. 10), and upper-level warming (Figs. 10 and 11) between 12 and 16 September, while the downshear quadrants experience similar increases primarily within the initial period of slow intensification (12–13 September). Having replaced RHLO (850–700-hPa RH averaged within a 200–800-km annulus) with upshear total precipitable water (TPW < 45 mm within a 500-km radius and within ±45° of the upshear SHIPS wind direction) in their enhanced SHIPS Rapid Intensification Index (SHIPS-RII) model, Kaplan et al. (2015) have already demonstrated the usefulness of upshear moisture content as a predictor of RI.

Intensification apparently also coincides with a decrease in the vertical tilt of the vortex; however, it is not clear whether this simply occurs due to a decrease in the strength of the VWSH between 13 and 14 September, or whether another mechanism such as the alignment of mid- and upper-level warming (section 6; Kerns and Chen 2015) or deep convection occurring in

the upshear quadrant (Stevenson et al. 2014; Rogers et al. 2015; Susca-Lopata et al. 2015) is responsible. As the mean RH profiles from the GH during the intensification stage (12 and 14–15 September) suggest (Fig. 9), in the upshear quadrants multiple relatively dry, subsiding layers are present in the middle (approximately 900–600 hPa) to upper troposphere (above 600 hPa). In the midtroposphere, these layers are likely associated with mesoscale downdrafts below the melting layer in lightly precipitating stratiform rain areas, whereby cooling from evaporation is overcome by dry adiabatic compression (i.e., an "onion" sounding; Zipser 1977) (Figs. 14 and 15). The removal of the relatively dry midtropospheric layers most likely occurs as the frequency, areal coverage, and rainfall rate of precipitation increases upshear—a conclusion that is not only supported by the evidence shown in Edouard (Figs. 5–7), but is also reinforced by multiple recent satellite studies of TC intensification (Kieper and Jiang 2012; Zagrodnik and Jiang 2014; Alvey et al. 2015; Tao and Jiang 2015). The increase in precipitation

symmetry can subsequently promote axisymmetric upper-level warming (Fig. 11) that favors intensification (deepening) of the vortex (Shapiro and Willoughby 1982; Nolan et al. 2007; Rogers 2010; Zhang and Chen 2012).

Alternatively, results on 12 September suggest that as long as the mesoscale downdrafts occur in close proximity to the developing low-level circulation center and are preferably aligned with the upper-tropospheric warming (Kerns and Chen 2015), subsidence warming in the low to midtroposphere can also favorably organize the nascent eye (Vigh 2010) and serve as a "reservoir of high $\theta_E$" to breed future deep convective growth in the eyewall (Dolling and Barnes 2012).

While the kinematic support will be offered in Part II, thermodynamic evidence that has been shown in this part of the study supports an azimuthal distribution of deep convection consistent with previous studies (e.g., Eastin et al. 2005; Hence and Houze 2011; Reasor et al. 2013; DeHart et al. 2014). Similar to the composite shown in Zhang et al. (2013), this distribution is intimately linked to the properties of the PBL, in which analyses (Fig. 13) indicate that the near-surface $\theta_E$ is maximized downshear right (favoring instability and initiation) and decreases in the left of shear quadrants as a result of cooling and drying from downdrafts (favoring stability and dissipation). The primary difference between the intensification and weakening stages is that the SSTs are sufficiently high ($>27°C$; Fig. 3) during intensification for surface fluxes to recover the relatively low-$\theta_E$ air as it passes cyclonically through the upshear right quadrant. During the weakening stage, cooling SSTs ($<26°C$) are unable to facilitate a recovery of low $\theta_E$ in the PBL.

Even though this study only examines a single case, results strongly suggest that the mechanisms responsible for intensification and weakening in Edouard are consistent with those previously hypothesized in satellite and in situ radar composite studies. Despite this agreement, the thermodynamic evolution must be examined in other cases for conclusions to be considered robust. While the NOAA and U.S. Air Force (USAF) WC-130J aircraft contribute to the vast majority of dropsonde data available in TCs, because those aircraft typically fly at and below 700 hPa, replicating analyses from this study would likely only be possible for a small sample of cases. This study has demonstrated one of the many invaluable benefits that a long endurance, high-altitude aircraft like the Global Hawk offers—its capability to provide full tropospheric dropsonde sampling at high spatial and temporal resolution, unique compared to the rest of the aircraft conventionally used for in situ TC sampling.

## REFERENCES

Abarca, S. F., K. L. Corbosiero, and T. J. Galarneau Jr., 2010: An evaluation of the Worldwide Lightning Location Network (WWLLN) using the National Lightning Detection Network (NLDN) as ground truth. *J. Geophys. Res.*, **115**, D18206, doi:10.1029/2009JD013411.

Alvey, G. R., III, J. Zawislak, and E. Zipser, 2015: Precipitation properties observed during tropical cyclone intensity change. *Mon. Wea. Rev.*, **143**, 4476–4492, doi:10.1175/MWR-D-15-0065.1.

Bender, M. A., 1997: The effect of relative flow on the asymmetric structure in the interior of hurricanes. *J. Atmos. Sci.*, **54**, 703–724, doi:10.1175/1520-0469(1997)054<0703:TEORFO>2.0.CO;2.

Black, M. L., J. F. Gamache, F. D. Marks Jr., C. E. Samsury, and H. E. Willoughby, 2002: Eastern Pacific Hurricanes Jimena of

1991 and Olivia of 1994: The effect of vertical shear on structure and intensity. *Mon. Wea. Rev.*, **130**, 2291–2312, doi:10.1175/1520-0493(2002)130<2291:EPHJOA>2.0.CO;2.

Bogner, P. B., G. M. Barnes, and J. L. Franklin, 2000: Conditional instability and shear for six hurricanes over the Atlantic Ocean. *Wea. Forecasting*, **15**, 192–207, doi:10.1175/1520-0434(2000)015<0192:CIASFS>2.0.CO;2.

Braun, S. A., 2010: Reevaluating the role of the Saharan air layer in Atlantic tropical cyclogenesis and evolution. *Mon. Wea. Rev.*, **138**, 2007–2037, doi:10.1175/2009MWR3135.1.

——, J. A. Sippel, and D. S. Nolan, 2012: The impact of dry midlevel air on hurricane intensity in idealized simulations with no mean flow. *J. Atmos. Sci.*, **69**, 236–257, doi:10.1175/JAS-D-10-05007.1.

——, and Coauthors, 2013: NASA's Genesis and Rapid Intensification Processes (GRIP) field experiment. *Bull. Amer. Meteor. Soc.*, **94**, 345–363, doi:10.1175/BAMS-D-11-00232.1.

——, P. A. Newman, and G. M. Heymsfield, 2016: NASA's Hurricane and Severe Storm Sentinel (HS3) investigation. *Bull. Amer. Meteor. Soc.*, doi:10.1175/BAMS-D-15-00186.1, in press.

Chen, H., and S. G. Gopalakrishnan, 2015: A study on the asymmetric rapid intensification of Hurricane Earl (2010) using the HWRF system. *J. Atmos. Sci.*, **72**, 531–550, doi:10.1175/JAS-D-14-0097.1.

Chen, S. S., J. A. Knaff, and F. D. Marks Jr., 2006: Effects of vertical wind shear and storm motion on tropical cyclone rainfall asymmetries deduced from TRMM. *Mon. Wea. Rev.*, **134**, 3190–3208, doi:10.1175/MWR3245.1.

Cione, J. J., P. G. Black, and S. H. Houston, 2000: Surface observations in the hurricane environment. *Mon. Wea. Rev.*, **128**, 1550–1561, doi:10.1175/1520-0493(2000)128<1550:SOITHE>2.0.CO;2.

Cram, T., J. Persing, M. Montgomery, and S. Braun, 2007: A Lagrangian trajectory view on transport and mixing processes between the eye, eyewall, and environment using a high-resolution simulation of Hurricane Bonnie (1998). *J. Atmos. Sci.*, **64**, 1835–1856, doi:10.1175/JAS3921.1.

DeHart, J. C., R. A. Houze Jr., and R. F. Rogers, 2014: Quadrant distribution of tropical cyclone inner-core kinematics in relation to environmental shear. *J. Atmos. Sci.*, **71**, 2713–2732, doi:10.1175/JAS-D-13-0298.1.

DeMaria, M., 1996: The effect of vertical shear on tropical cyclone intensity change. *J. Atmos. Sci.*, **53**, 2076–2088, doi:10.1175/1520-0469(1996)053<2076:TEOVSO>2.0.CO;2.

——, M. Mainelli, L. K. Shay, J. A. Knaff, and J. Kaplan, 2005: Further improvements to the Statistical Hurricane Intensity Prediction Scheme (SHIPS). *Wea. Forecasting*, **20**, 531–543, doi:10.1175/WAF862.1.

Dolling, K., and G. M. Barnes, 2012: Warm-core formation in Tropical Storm Humberto (2001). *Mon. Wea. Rev.*, **140**, 1177–1190, doi:10.1175/MWR-D-11-00183.1.

——, and ——, 2014: The evolution of Hurricane Humberto (2001). *J. Atmos. Sci.*, **71**, 1276–1291, doi:10.1175/JAS-D-13-0164.1.

Dunion, J. P., and C. S. Velden, 2004: The impact of the Saharan air layer on Atlantic tropical cyclone activity. *Bull. Amer. Meteor. Soc.*, **85**, 353–365, doi:10.1175/BAMS-85-3-353.

——, C. Thorncroft, and C. S. Velden, 2014: The tropical cyclone diurnal cycle of mature hurricanes. *Mon. Wea. Rev.*, **142**, 3900–3919, doi:10.1175/MWR-D-13-00191.1.

Durden, S. L., 2013: Observed tropical cyclone eye thermal anomaly profiles extending above 300 hPa. *Mon. Wea. Rev.*, **141**, 4256–4268, doi:10.1175/MWR-D-13-00021.1.

Eastin, M. D., W. M. Gray, and P. G. Black, 2005: Buoyancy of convective vertical motions in the inner core of intense

hurricanes. Part II: Case studies. *Mon. Wea. Rev.*, **133**, 209–227, doi:10.1175/MWR-2849.1.

Frank, W. M., and E. A. Ritchie, 1999: Effects of environmental flow upon tropical cyclone structure. *Mon. Wea. Rev.*, **127**, 2044–2061, doi:10.1175/1520-0493(1999)127<2044:EOEFUT>2.0.CO;2.

——, and ——, 2001: Effects of vertical wind shear on the intensity and structure of numerically simulated hurricanes. *Mon. Wea. Rev.*, **129**, 2249–2269, doi:10.1175/1520-0493(2001)129<2249:EOVWSO>2.0.CO;2.

Gray, W. M., 1968: Global view of the origin of tropical disturbances and storms. *Mon. Wea. Rev.*, **96**, 669–700, doi:10.1175/1520-0493(1968)096<0669:GVOTOO>2.0.CO;2.

Guimond, S. R., G. M. Heymsfield, and F. J. Turk, 2010: Multiscale observations of Hurricane Dennis (2005): The effects of hot towers on rapid intensification. *J. Atmos. Sci.*, **67**, 633–654, doi:10.1175/2009JAS3119.1.

Hence, D. A., and R. A. Houze Jr., 2011: Vertical structure of hurricane eyewalls as seen by the TRMM Precipitation Radar. *J. Atmos. Sci.*, **68**, 1637–1652, doi:10.1175/2011JAS3578.1.

Houze, R. A., Jr., 2010: Clouds in tropical cyclones. *Mon. Wea. Rev.*, **138**, 293–344, doi:10.1175/2009MWR2989.1.

Jiang, H., 2012: The relationship between tropical cyclone intensity change and the strength of inner-core convection. *Mon. Wea. Rev.*, **140**, 1164–1176, doi:10.1175/MWR-D-11-00134.1.

Jones, S. C., 1995: The evolution of vortices in vertical shear. I: Initially barotropic vortices. *Quart. J. Roy. Meteor. Soc.*, **121**, 821–851, doi:10.1002/qj.49712152406.

Kaplan, J., and M. DeMaria, 2003: Large-scale characteristics of rapidly intensifying tropical cyclones on the North Atlantic basin. *Wea. Forecasting*, **18**, 1093–1108, doi:10.1175/1520-0434(2003)018<1093:LCORIT>2.0.CO;2.

——, and Coauthors, 2015: Evaluating environmental impacts on tropical cyclone rapid intensification predictability utilizing statistical models. *Wea. Forecasting*, **30**, 1374–1396, doi:10.1175/WAF-D-15-0032.1.

Kelley, O. A., J. Stout, and J. B. Halverson, 2004: Tall precipitation cells in tropical cyclones eyewalls are associated with tropical cyclone intensification. *Geophys. Res. Lett.*, **31**, L24112, doi:10.1029/2004GL021616.

Kerns, B. W., and S. S. Chen, 2015: Subsidence warming as an underappreciated ingredient in tropical cyclogenesis. Part I: Aircraft observations. *J. Atmos. Sci.*, **72**, 4237–4260, doi:10.1175/JAS-D-14-0366.1.

Kieper, M., and H. Jiang, 2012: Predicting tropical cyclone rapid intensification using the 37 GHz ring pattern identified from passive microwave measurements. *Geophys. Res. Lett.*, **39**, L13804, doi:10.1029/2012GL052115.

Kossin, J. P., 2002: Daily hurricane variability inferred from GOES infrared imagery. *Mon. Wea. Rev.*, **130**, 2260–2270, doi:10.1175/1520-0493(2002)130<2260:DHVIFG>2.0.CO;2.

——, and M. D. Eastin, 2001: Two distinct regimes in the kinematic and thermodynamic structure of the hurricane eye and eyewall. *J. Atmos. Sci.*, **58**, 1079–1090, doi:10.1175/1520-0469(2001)058<1079:TDRITK>2.0.CO;2.

——, and W. H. Schubert, 2001: Mesovortices, polygonal flow patterns, and rapid pressure falls in hurricane-like vortices. *J. Atmos. Sci.*, **58**, 2196–2209, doi:10.1175/1520-0469(2001)058<2196:MPFPAR>2.0.CO;2.

Marks, F. D., Jr., and L. K. Shay, 1998: Landfalling tropical cyclones: Forecast problems and associated research opportunities. *Bull. Amer. Meteor. Soc.*, **79**, 305–323, doi:10.1175/1520-0477(1998)079<0305:LTCFPA>2.0.CO;2.

——, R. A. Houze Jr., and J. F. Gamache, 1992: Dual-aircraft investigation of the inner core of Hurricane Norbert. Part I: Kinematic structure. *J. Atmos. Sci.*, **49**, 919–942, doi:10.1175/1520-0469(1992)049<0919:DAIOTI>2.0.CO;2.

Merrill, R. T., 1988: Environmental influences on hurricane intensification. *J. Atmos. Sci.*, **45**, 1678–1687, doi:10.1175/1520-0469(1988)045<1678:EIOHI>2.0.CO;2.

Molinari, J., and D. Vollaro, 2010: Rapid intensification of a sheared tropical storm. *Mon. Wea. Rev.*, **138**, 3869–3885, doi:10.1175/2010MWR3378.1.

——, ——, and K. L. Corbosiero, 2004: Tropical cyclone formation in a sheared environment: A case study. *J. Atmos. Sci.*, **61**, 2493–2509, doi:10.1175/JAS3291.1.

——, P. Dodge, D. Vollaro, K. L. Corbosiero, and F. Marks Jr., 2006: Mesoscale aspects of the downshear reformation of a tropical cyclone. *J. Atmos. Sci.*, **63**, 341–354, doi:10.1175/JAS3591.1.

——, D. M. Romps, D. Vollaro, and L. Nguyen, 2012: CAPE in tropical cyclones. *J. Atmos. Sci.*, **69**, 2452–2463, doi:10.1175/JAS-D-11-0254.1.

——, J. Frank, and D. Vollaro, 2013: Convective bursts, downdraft cooling, and boundary layer recovery in a sheared tropical storm. *Mon. Wea. Rev.*, **141**, 1048–1060, doi:10.1175/MWR-D-12-00135.1.

NASA GSFC, 2010: Precipitation Processing System (PPS) Algorithm Theoretical Basis Document (ATBD): NASA GPM level 1C algorithms, version 1.0. NASA GSFC, Greenbelt, MD, 39 pp. [Available online at https://pmm.nasa.gov/sites/default/files/document_files/L1C_ATBD_v1.pdf.]

Nguyen, L. T., and J. Molinari, 2012: Rapid intensification of a sheared, fast-moving hurricane over the Gulf Stream. *Mon. Wea. Rev.*, **140**, 3361–3378, doi:10.1175/MWR-D-11-00293.1.

Nolan, D. S., and L. D. Grasso, 2003: Nonhydrostatic, three-dimensional perturbations to balanced, hurricane-like vortices. Part II: Symmetric response and nonlinear simulations. *J. Atmos. Sci.*, **60**, 2717–2745, doi:10.1175/1520-0469(2003)060<2717:NTPTBH>2.0.CO;2.

——, Y. Moon, and D. P. Stern, 2007: Tropical cyclone intensification from asymmetric convection: Energetics and efficiency. *J. Atmos. Sci.*, **64**, 3377–3405, doi:10.1175/JAS3988.1.

Ooyama, K., 1969: Numerical simulation of the life cycle of tropical cyclones. *J. Atmos. Sci.*, **26**, 3–40, doi:10.1175/1520-0469(1969)026<0003:NSOTLC>2.0.CO;2.

——, 1982: Conceptual evolution of the theory and modeling of the tropical cyclone. *J. Meteor. Soc. Japan*, **60**, 369–379.

Reasor, P. D., and M. D. Eastin, 2012: Rapidly intensifying Hurricane Guillermo (1997). Part II: Resilience in shear. *Mon. Wea. Rev.*, **140**, 425–444, doi:10.1175/MWR-D-11-00080.1.

——, ——, and J. F. Gamache, 2009: Rapidly intensifying Hurricane Guillermo (1997). Part I: Low-wavenumber structure and evolution. *Mon. Wea. Rev.*, **137**, 603–631, doi:10.1175/2008MWR2487.1.

——, R. Rogers, and S. Lorsolo, 2013: Environmental flow impacts on tropical cyclone structure diagnosed from airborne Doppler radar composites. *Mon. Wea. Rev.*, **141**, 2949–2969, doi:10.1175/MWR-D-12-00334.1.

Riemer, M., M. T. Montgomery, and M. E. Nicholls, 2010: A new paradigm for intensity modification of tropical cyclones: Thermodynamic impact of vertical wind shear on the inflow layer. *Atmos. Chem. Phys.*, **10**, 3163–3188, doi:10.5194/acp-10-3163-2010.

Rodgers, E. B., W. S. Olson, V. M. Karyampudi, and H. F. Pierce, 1998: Satellite-derived latent heating distribution and environmental influences in Hurricane Opal (1995). *Mon. Wea. Rev.*, **126**, 1229–1247, doi:10.1175/1520-0493(1998)126<1229:SDLHDA>2.0.CO;2.

Rogers, R., 2010: Convective-scale structure and evolution during a high-resolution simulation of tropical cyclone rapid intensification. *J. Atmos. Sci.*, **67**, 44–70, doi:10.1175/2009JAS3122.1.

——, and Coauthors, 2006: The Intensity Forecasting Experiment: A NOAA multiyear field program for improving tropical cyclone intensity forecasts. *Bull. Amer. Meteor. Soc.*, **87**, 1523–1537, doi:10.1175/BAMS-87-11-1523.

——, P. Reasor, and S. Lorsolo, 2013a: Airborne Doppler observations of the inner-core structural differences between intensifying and steady-state tropical cyclones. *Mon. Wea. Rev.*, **141**, 2970–2991, doi:10.1175/MWR-D-12-00357.1.

——, and Coauthors, 2013b: NOAA's Hurricane Intensity Forecasting Experiment: A progress report. *Bull. Amer. Meteor. Soc.*, **94**, 859–882, doi:10.1175/BAMS-D-12-00089.1.

——, P. Reasor, and J. Zhang, 2015: Multiscale structure and evolution of Hurricane Earl (2010) during rapid intensification. *Mon. Wea. Rev.*, **143**, 536–562, doi:10.1175/MWR-D-14-00175.1.

——, J. Zhang, J. Zawislak, H. Jiang, G. R. Alvey III, E. J. Zipser, and S. N. Stevenson, 2016: Observations of the structure and evolution of Hurricane Edouard (2014) during intensity change. Part II: Kinematic structure and the distribution of deep convection. *Mon. Wea. Rev.*, **144**, 3355–3376, doi:10.1175/MWR-D-16-0017.1.

Rozoff, C. M., C. S. Velden, J. Kaplan, J. P. Kossin, and A. J. Wimmers, 2015: Improvements in the probabilistic prediction of tropical cyclone rapid intensification with passive microwave observations. *Wea. Forecasting*, **30**, 1016–1038, doi:10.1175/WAF-D-14-00109.1.

Rudlosky, S. D., and D. T. Shea, 2013: Evaluation WWLLN performance relative to TRMM/LIS. *Geophys. Res. Lett.*, **40**, 2344–2348, doi:10.1002/grl.50428.

Schubert, W. H., and J. J. Hack, 1982: Inertial stability and tropical cyclone development. *J. Atmos. Sci.*, **39**, 1687–1697, doi:10.1175/1520-0469(1982)039<1687:ISATCD>2.0.CO;2.

——, M. T. Montgomery, R. K. Taft, T. A. Guinn, S. R. Fulton, J. P. Kossin, and J. P. Edwards, 1999: Polygonal eyewalls, asymmetric eye contraction, and potential vorticity mixing in hurricanes. *J. Atmos. Sci.*, **56**, 1197–1223, doi:10.1175/1520-0469(1999)056<1197:PEAECA>2.0.CO;2.

Shapiro, L. J., and H. E. Willoughby, 1982: The response of balanced hurricanes to local sources of heat and momentum. *J. Atmos. Sci.*, **39**, 378–394, doi:10.1175/1520-0469(1982)039<0378:TROBHT>2.0.CO;2.

Shay, L. K., P. G. Black, A. J. Mariano, J. D. Hawkins, and R. L. Elsberry, 1992: Upper-ocean response to Hurricane Gilbert. *J. Geophys. Res.*, **97**, 20 227–20 248, doi:10.1029/92JC01586.

Shu, S., and L. Wu, 2009: Analysis of the influence of the Saharan air layer on tropical cyclone intensity using AIRS/Aqua data. *Geophys. Res. Lett.*, **36**, L09809, doi:10.1029/2009GL037634.

Sippel, J. A., S. A. Braun, and C.-L. Shie, 2011: Environmental influences on the strength of Tropical Storm Debby (2006). *J. Atmos. Sci.*, **68**, 2557–2581, doi:10.1175/2011JAS3648.1.

Spencer, R. W., H. M. Goodman, and R. E. Hood, 1989: Precipitation retrieval over land and ocean with the SSM/I: Identification and characteristics of the scattering signal. *J. Atmos. Oceanic Technol.*, **6**, 254–273, doi:10.1175/1520-0426(1989)006<0254:PROLAO>2.0.CO;2.

Stern, D. P., and D. S. Nolan, 2012: On the height of the warm core in tropical cyclones. *J. Atmos. Sci.*, **69**, 1657–1680, doi:10.1175/JAS-D-11-010.1.

Stevenson, S. N., K. L. Corbosiero, and J. Molinari, 2014: The convective evolution and rapid intensification of Hurricane Earl (2010). *Mon. Wea. Rev.*, **142**, 4364–4380, doi:10.1175/MWR-D-14-00078.1.

——, ——, and S. F. Abarca, 2016: Lightning in eastern North Pacific tropical cyclones: A comparison to the North Atlantic. *Mon. Wea. Rev.*, **144**, 225–239, doi:10.1175/MWR-D-15-0276.1.

Stewart, S. R., 2014: National Hurricane Center tropical cyclone report: Hurricane Edouard. Rep. AL062014, National Hurricane Center, 19 pp. [Available online at http://www.nhc.noaa.gov/data/tcr/AL062014_Edouard.pdf.]

Susca-Lopata, G., J. Zawislak, E. Zipser, and R. Rogers, 2015: The role of observed environmental conditions and precipitation evolution in the rapid intensification of Hurricane Earl (2010). *Mon. Wea. Rev.*, **143**, 2207–2223, doi:10.1175/MWR-D-14-00283.1.

Tao, C., and H. Jiang, 2015: Distributions of shallow to very deep precipitation–convection in rapidly intensifying tropical cyclones. *J. Climate*, **28**, 8791–8824, doi:10.1175/JCLI-D-14-00448.1.

UCAR/NCAR Earth Observing Laboratory, 2015: HS3 2014 Global Hawk dropsonde data, version 1.0. UCAR/NCAR Earth Observing Laboratory, accessed 27 April 2015, doi:10.5065/D6GB2243. [Available online at https://data.eol.ucar.edu/dataset/348.004.]

Uhlhorn, E. W., B. W. Klotz, T. Vukicevic, P. D. Reasor, and R. F. Rogers, 2014: Observed hurricane wind speed asymmetries and relationships to motion and environmental shear. *Mon. Wea. Rev.*, **142**, 1290–1311, doi:10.1175/MWR-D-13-00249.1.

Vigh, J. L., 2010: Formation of the hurricane eye. Ph.D. dissertation, Dept. of Atmospheric Science, Colorado State University, Fort Collins, CO, 538 pp.

Wentz, F. J., C. L. Gentemann, D. K. Smith, and D. Chelton, 2000: Satellite measurements of sea surface temperature through clouds. *Science*, **288**, 847–850, doi:10.1126/science.288.5467.847.

Young, K., T. Hock, and C. Martin, 2016: HS3-2014 dropsonde data quality report. National Center for Atmospheric Research, Earth Observing Laboratory, 11 pp. [Available online at http://data.eol.ucar.edu/datafile/nph-get/348.004/readme.V2.HS3-2014.GHdropsonde.pdf.]

Zagrodnik, J. P., and H. Jiang, 2014: Rainfall, convection, and latent heating distributions in rapidly intensifying tropical cyclones. *J. Atmos. Sci.*, **71**, 2789–2809, doi:10.1175/JAS-D-13-0314.1.

Zhang, D.-L., and H. Chen, 2012: Importance of the upper-level warm core in the rapid intensification of a tropical cyclone. *Geophys. Res. Lett.*, **39**, L02806, doi:10.1029/2012GL052355.

——, and L. Zhu, 2012: Roles of upper-level processes in tropical cyclogenesis. *Geophys. Res. Lett.*, **39**, L17804, doi:10.1029/2012GL052355.

Zhang, J. A., R. F. Rogers, P. D. Reasor, E. W. Uhlhorn, and F. D. Marks Jr., 2013: Asymmetric hurricane boundary layer structure from dropsonde composites in relation to the environmental vertical wind shear. *Mon. Wea. Rev.*, **141**, 3968–3984, doi:10.1175/MWR-D-12-00335.1.

Zipser, E. J., 1977: Mesoscale and convective-scale downdrafts as distinct components of squall-line circulation. *Mon. Wea. Rev.*, **105**, 1568–1589, doi:10.1175/1520-0493(1977)105<1568:MACDAD>2.0.CO;2.